Received: 9 September 2023 | Revised: 13 November 2023 | Accepted: 6 December 2023

DOI: 10.1111/jnc.16042

Journal of Neurochemistry JNC The Official Journal of the International Society for Neurochemistry WILEY

ORIGINAL ARTICLE

Mass spectrometry imaging highlights dynamic patterns of lipid co-expression with Aβ plaques in mouse and human brains

Helen Xuexia Huang[1,2] | Paolo Inglese[1,3] | Jiabin Tang[4] | Riad Yagoubi[1,2] | Gonçalo D. S. Correia[1,3] | Verena M. Horneffer-van der Sluis[3] | Stephane Camuzeaux[3] | Vincen Wu[1] | Maksym V. Kopanitsa[2] | Nanet Willumsen[2,4] | Johanna S. Jackson[2,4] | Anna M. Barron[5] | Takashi Saito[6,7] | Takaomi C. Saido[6,7] | Steve Gentlemen[4] | Zoltan Takats[1] | Paul M. Matthews[2,4]

[1]Section of Bioanalytical Chemistry, Department of Metabolism, Digestion and Reproduction, Imperial College London, London, UK

[2]UK Dementia Research Institute at Imperial College London, Imperial College London, London, UK

[3]National Phenome Centre, Department of Metabolism, Digestion and Reproduction, Imperial College London, London, UK

[4]Department of Brain Sciences, Imperial College London, London, UK

[5]Lee Kong Chian School of Medicine, Nanyang Technological University, Singapore, Singapore

[6]Laboratory for Proteolytic Neuroscience, RIKEN Center for Brain Science, Saitama, Japan

[7]Department of Neurocognitive Science, Institute of Brain Science, Nagoya City University, Graduate School of Medical Sciences, Nagoya, Aichi, Japan

Correspondence
Zoltan Takats, Section of Bioanalytical Chemistry, Department of Metabolism, Digestion and Reproduction, Imperial College London, Hammersmith Campus, London SW7 2AZ, UK.

Email: z.takats@imperial.ac.uk

Paul M. Matthews, UK Dementia Research Institute at Imperial College London, Imperial College London, Uren Building, White City Campus, London W12 0BZ, UK.
Email: p.matthews@imperial.ac.uk

Funding information
UK Dementia Research Institute

Abstract

Lipids play crucial roles in the susceptibility and brain cellular responses to Alzheimer's disease (AD) and are increasingly considered potential soluble biomarkers in cerebrospinal fluid (CSF) and plasma. To delineate the pathological correlations of distinct lipid species, we conducted a comprehensive characterization of both spatially localized and global differences in brain lipid composition in App^{NL-G-F} mice with spatial and bulk mass spectrometry lipidomic profiling, using human amyloid-expressing (h-Aβ) and WT mouse brains controls. We observed age-dependent increases in lysophospholipids, bis(monoacylglycerol) phosphates, and phosphatidylglycerols around Aβ plaques in App^{NL-G-F} mice. Immunohistology-based co-localization identified associations between focal pro-inflammatory lipids, glial activation, and autophagic flux disruption. Likewise, in human donors with varying Braak stages, similar studies of

Abbreviations: ABC, ATP-binding cassette; AD, Alzheimer's Disease; *APP*, amyloid precursor protein; ATP, adenosine triphosphate; *Aβ*, amyloid-*β*; BMP, Bis(monoacylglycerol) phosphate; BSA, bovine serum albumin; CD68, cluster of differentiation 68; CSF, cerebrospinal fluid; DESI, desorption electrospray ionization; DG, diglyceride; DHA, docosahexaenoic acid; ESI, electrospray ionization; FA, fatty acid; FAD, familial Alzheimer's disease; GC, gas chromatography; GFAP, glial fibrillary acidic protein; IHC, immunohistochemistry; IMC, imaging mass cytometry; IPA, isopropyl alcohol; LAMP1, lysosomal-associated membrane protein 1; LC, liquid chromatography; LPA, lysophosphatidic acid; LPC, Lysophosphatidylcholine; LPE, Lysophosphatidylethanolamine; LPG, Lysophosphatidylglycerol; LPI, Lysophosphatidylinositol; LPL, Lysophospholipid; MALDI, matrix-assisted laser desorption/ionization; MFSD2A, major facilitator superfamily domain-containing protein 2A; MS, mass spectrometry; MSI, mass spectrometry imaging; MW, molecular weight; *NMR*, nuclear magnetic resonance; PA, phosphatidic acid; PAF, platelet-activating factor; PC, phosphatidylcholine; PE, phosphatidylethanolamine; PEM, plaque-enriched module; PG, phosphatidylglycerol; PI, phosphatidylinositol; PLA2, phospholipase A2; PMD, post mortem delay; PS, phosphatidylserine; PUFA, polyunsaturated fatty acids; ROI, region of interest; RRID, research resource identifiers; SNN, shared nearest neighbor; SR, study reference; TG, triglyceride; TOF, time of flight; UPLC, ultra-performance liquid chromatography.

Helen Xuexia Huang and Paolo Inglese contributed equally to this work.

This article is accompanied by an Editorial Highlight "Lipid imaging of Alzheimer's disease pathology" on page 1175.

cortical sections revealed co-expression of lysophospholipids and ceramides around Aβ plaques in AD (Braak stage V/VI) but not in earlier Braak stage controls. Our findings in mice provide evidence of temporally and spatially heterogeneous differences in lipid composition as local and global Aβ-related pathologies evolve. Observing similar lipidomic changes associated with pathological Aβ plaques in human AD tissue provides a foundation for understanding differences in CSF lipids with reported clinical stage or disease severity.

KEYWORDS
Alzheimer's disease, autophagic disruption, Aβ plaques, network analysis, pro-inflammatory lipids, spatial lipidomics

1 | INTRODUCTION

Variants associated with AD risk have been reported in or near genes encoding lipoproteins (A1 (Slot et al., 2017), A4 (Yamazaki et al., 2019), B (Picard et al., 2021), C1 (Petit-Turcotte et al., 2001), C3 (Shih et al., 2014), E4 (Mahley et al., 2006), and clusterin (Bertrand et al., 1995)) and many ATP-binding cassette (ABC) transporters, including ABCA transporters (e.g., A1 (Wahrle et al., 2008), A2 (Mace et al., 2005), A7 (Steinberg et al., 2015)) and ABCG transporters (G1 (Sano et al., 2016), G2 (Xiong et al., 2009), G4 (Sano et al., 2016)). The significant number of genes linked to lipid metabolism associated with Alzheimer's disease (AD) risk suggests an essential role for lipid homeostasis pathologies in AD pathogenesis (Jansen et al., 2019). Lipids are major components of cellular membranes and modulators of membrane-associated functions, including Aβ plaque formation (Miller et al., 2020) and inflammatory signaling (Miller et al., 2020). It has also been shown that different classes of lipids play significant roles in aging (Svennerholm et al., 1994). Oligomeric Aβ has been shown to disrupt lipid homeostasis (e.g., phosphorylated phosphatidylinositols (PIs), which act as secondary messengers in multiple cells to regulate actin remodeling, phagocytosis, and other cell functions) (Berman et al., 2008). Brain lipid composition and soluble lipids found in cerebrospinal fluid (CSF) or plasma change with disease (Byeon et al., 2021a; Fonteh et al., 2020). Pathological Aβ expression triggers a cascade of dynamic brain cellular responses characterized by neuroinflammatory glial activation. In pre-clinical models, this is reflected in age-dependent heterogeneity of cellular pathology in and around individual plaques, even in the same brain (Sasaguri et al., 2017).

To characterize lipidomic changes with increasing comprehensiveness, analyses of bulk tissue homogenates are being conducted using liquid (LC) and gas chromatographic (GC) mass spectrometry (MS). This body of work is leading toward a mechanistic understanding of lipidome/metabolome alterations in AD (Barupal et al., 2019; Byeon et al., 2021b; Proitsi et al., 2017). While cell-specific AD metabolomic studies have been carried out in vitro (Gao et al., 2017), limited data have been available to spatially resolve the relationships between specific lipidomic changes and cellular pathologies in tissues. Matrix-assisted laser desorption/ionization mass spectrometry imaging (MALDI MSI) allows relatively high-resolution mapping of lipids, but matrix deposition is destructive, making it difficult to directly co-register lipidomic features detected with cellular markers (Aichler & Walch, 2015). In contrast, desorption electrospray ionization (DESI) allows the spatial distribution mapping of biological molecules (lipids, small molecules, drugs, and proteins (Takats et al., 2004)) based on the production of ions for mass spectrometry that is generated by impacting a tissue surface with a charged solvent spray (Ambrose et al., 2017). DESI is a non-destructive method, enabling immunohistology on the same sections for accurate co-localization with cellular anatomical and pathological features (Strittmatter et al., 2022).

In this study, we combined spatial and bulk MS methods to characterize associated age-related spatial heterogeneity of lipidomic pathology in the brains of $App^{NL\text{-}G\text{-}F}$, humanized Aβ (h-Aβ), and age−/sex-matched wild-type (WT) mice. The aim was to distinguish generalized from localized lipidomic changes occurring in or near Aβ plaques. We were able to co-localize Aβ-related cellular pathology, describe correlations between pathological features and lipids, and refine hypotheses concerning the mechanisms by which specific classes of lipids in CSF and blood, proposed as possible biomarkers for AD, arise (Byeon et al., 2021a; Fonteh et al., 2020).

2 | MATERIALS AND METHODS

2.1 | Animals

The $APP^{NL\text{-}G\text{-}F}$ mouse model includes a humanized Aβ region (676RHDSGYEV684), with 3 mutations (the Swedish: KM670/671NL (Sturchler-Pierrat et al., 1997); the Artic: E693G (Dahlgren et al., 2002; Nilsberth et al., 2001); the Iberian: I716F (Lichtenthaler et al., 1999)) knocked in using CRISPR/Cas9. Homozygous $App^{NL\text{-}G\text{-}F}$ mice (strain name: $App^{tm3.1Tcs/Apptm3.1Tcs}$, RRID:MGI:5638675, $n = 6$: three females and three males) and wild-type C57BL/6J mice (RRID:IMSR_JAX:000664) ($n = 6$: three females and three males) were housed at

the Lee Kong Chian School of Medicine Animal Research Facilities. Mice were maintained on a 12/12 h light/dark cycle in a group with sex-matched littermates (maximum 5 mice per cage) in individually ventilated cage racks with drinking nozzles attached to the individual cage to allow ad libitum access to reverse osmosis-purified water and food (standard laboratory diet of irradiated 1324 pellets, Altromin Spezialfutter GmbH, Lage, Germany). While an alternative protocol for rapid in situ fixation using high energy head-focused microwave prior snap freezing has been proposed (Juras et al., 2023), we used the more frequently reported approach for MSI studies of snap freezing (Kaya et al., 2017, 2018a, 2020, 2023). Mice that were 2.5, 7, or 12 months old and did not undergo any other procedures received an intraperitoneal injection of sodium pentobarbital (200 mg/kg, Jurox). After the loss of the pedal reflex, the animals were killed by decapitation, and their brains were quickly dissected free over ice, snap-frozen in individual Eppendorf tubes in liquid nitrogen, and stored at −80°C. Subsequently, the brain samples were shipped on dry ice to the Department of Metabolism, Digestion, and Reproduction at Imperial College, London, UK for studies of the tissue blocks. All experiments were carried out in accordance with the National Advisory Committee for Laboratory Animal Research guidelines and approved by the by the NTU Institutional Animal Care and Use Committee (IACUC# A0384).

We used brain tissue from $App^{hu/hu}$ mice (strain name: $App^{em1Bdes}$, $n = 3$: all males, referred to in the main article as h-Aβ) expressing the common human *APP* allele as a control for expression of the variant form. The $App^{hu/hu}$ mice also were fed with the standard laboratory diet and Brain tissue was prepared in similar ways to that outlined above in Prof Bart de Strooper's lab at the University of Leuven (KU Leuven), where they were generated (Serneels et al., 2020). The protocol for generation and sacrifice of the animals was approved by the Ethical Committee for Animal Experimentation at the University of Leuven (KU Leuven).

The number of brain samples used was estimated based on similar MSI studies (Kaya et al., 2017, 2018a; Michno et al., 2018, 2022). The experiment was not blinded to the origin of the brain tissue samples to enable control and amyloid model tissues within each study to be interleaved for analysis to limit batch effects.

2.2 | Human brain tissue samples

We obtained cases from the Newcastle Brain Tissue Resource, a part of the Brains for Dementia Research Network. We selected entorhinal and somatosensory cortex (EC) samples from 6 non-diseased control (NDC) cases (Braak stage 0-II) and 6 Alzheimer's disease (AD) cases (Braak stage III-VI), resulting in a total of 24 brain samples (Table S1, online resource). The criteria for brain sample selection included: (1) no prior exposure to commonly used embedding material OCT; (2) late-onset Alzheimer's disease or the absence of neuropathology confirmed through neuropathological analyses; (3) relatively short post mortem delay (PMD; <48 h). Frozen blocks were cryo-sectioned at 10 μm, and both blocks and sections were stored at −80°C for subsequent analyses. The human study was carried out in accordance with the Regional Ethics Committee and Imperial College Use of Human Tissue guidelines. The human tissue came from brain banks that are part of the UK Brain Banks Network. All the brain banks in the Network have generic ethics committee approval to function as research tissue banks, which means that they can provide tissue samples to UK-based researchers for a broad range of studies without the need for the researchers to obtain their own ethics approval.

2.3 | Tissue sectioning

Mouse brains were embedded using a matrix based on 2% hydroxypropyl methylcellulose (40–60 cP, 2% in H_2O, Sigma-Aldrich, Cat# H8384, CAS: 9004-65-3) and polyvinylpyrrolidone (average MW 360000) (Sigma-Aldrich, Cat# PVP360, CAS: 9003-39-8) as previously described (Dannhorn et al., 2020). The embedded tissue blocks were coronally cryo-sectioned at 10 μm thickness (sections collected from coronal Level 73–84, Allen Reference Atlas). Cryosectioning was performed using a Thermo Scientific™ Cryotome™ FSE cryostat, with chamber temperature set to −20°C and sample temperature at −18°C. The sections were then thaw-mounted onto SuperFrost glass slides (Thermo Scientific™ SuperFrost™ Microscope Slides, Ground 90°, Thermo Fisher Scientific Inc., Waltham, MA, USA). Subsequently, the sections were dried using a nitrogen flow, vacuum-sealed, and stored at −80°C until further analysis.

2.4 | DESI MSI

DESI-MSI was performed using a Xevo-G2XS mass spectrometer coupled with an Acquity UPLC (Waters, Milford, MA, USA) operated in sensitivity mode. The DESI ion source and a two-dimensional DESI stage were obtained from Prosolia (Indianapolis, IN, USA). The custom-built inlet capillary was heated to 270°C. The DESI MSI experiments covered the mass range of 50–1000 in both positive and negative ion modes, using a spray solvent (MeOH: H_2O = 95: 5) at a flow rate of 1.5 μL/min. The DESI source parameters were optimized on standard pork liver tissue for optimal sensitivity, with settings including a spray voltage of 4.5 kV, a sprayer-to-surface distance of 1.5 mm, a sprayer-to-inlet distance of 8 mm, a spray impact angle of 75°, a collection angle of 10°, and nebulizing gas (N_2) pressure set to 4 bar at a flow rate of 1.5 μL/min. The MS parameters included a scan time of 0.186 s, a source temperature of 150°C, a sampling cone voltage of −40 V, and a source offset of −80 V. The tissue surface was scanned horizontally at a rate of 75 μm/s with a 75 μm vertical step, covering the entire tissue area. The sprayer head remained grounded throughout the run. For experiments with a resolution of 25 μm, the flow rate was adjusted to 0.3 μL/min, and sprayer-to-inlet distance was adjusted to 3 mm without other significant alterations to the sprayer geometry. For all the MSI experiment run orders, a simple randomization using Excel was performed.

2.5 | Immunohistochemistry

Following DESI analysis, tissue sections were fixed in a mixture of acetone and MeOH (1:1) at −20°C for 10 min and then air-dried at room temperature for 20 min. No antigen retrieval was performed. Blocking reagent containing normal horse serum was used, and endogenous peroxidase activity was blocked using 0.3% H_2O_2 in phosphate-buffered saline (PBS). Samples were incubated overnight at 4°C with the primary antibody (anti-amyloid fibril antibody [mOC87], Abcam, Cat#ab201062, 1:1000 dilution). Other primary antibodies used include Anti-LAMP1 (Abcam, Cat#ab208943, RRID:AB_2923327), Anti-Glial Fibrillary Acidic Protein (Dako, Cat# Z0334, RRID:AB_10013382) and anti-mouse CD68 (Biolegend, Cat#137001, RRID:AB_2044003). All primary antibodies were absorbed in 7.5% bovine serum albumin (BSA), diluted in PBS-T. After thorough washing, the secondary antibody was applied at room temperature for 30 min, and the slides were exposed to 3′3-diaminobenzidine (DAB) for 1 minute using an ImmPact kit (ImmPACT® DAB Substrate, horseradish peroxidase, Vector Laboratories, Cat# SK-4105). Subsequently, the slides were counterstained with hematoxylin, dehydrated, cleared, and mounted. For quantification, hemispheres fixed in PFA were used. Sections were air-dried for at least 1 h, followed by three PBS changes (5 min each), and then processed as described above. No antigen retrieval was required.

2.6 | Imaging mass cytometry (IMC) of post-DESI and fresh frozen tissues

We used IMC histology to correlate lipid features from DESI MSI with key AD markers. Post-DESI and adjacent tissues were briefly fixed with 1% PFA for 10 min at 4°C, followed by cold methanol treatment for 5 min at −20°C (Guo et al., 2020). The tissues were then air-dried for 20 min at room temperature, rehydrated in PBS for 15 min, and blocked with 3% BSA for 3 h at room temperature. A cocktail of antibodies was diluted in 0.3% BSA in PBS-T and applied to the tissue for overnight incubation at 4°C. Following PBS rinses, the sections were counterstained with 125 nM Maxpar® Intercalator-Ir (Fluidigm) in PBS for 45 min at room temperature. After additional PBS rinses, the sections were air-dried for 2 h at room temperature. Antibody-labeled tissues were raster-ablated using a Hyperion™ Laser Scanning Module (Fluidigm) with a 1 μm diameter spot size at 200 Hz. CyTOF Software (Fluidigm, version 6.7) was used to acquire images for each antibody channel. The exported raw 16-bit tiff images were then subjected to further analysis using ImageJ Fiji.

2.7 | IHC and IMC statistical analyses

Cell counting and area measurements were performed using Halo v2.1. Statistical analyses were carried out using GraphPad Prism 8.4 software. For co-localization quantification, we utilized JACOP (Bolte & Cordelieres, 2006) in ImageJ Fiji. Because of the relatively noisy background, automatic thresholding of the images was applied.

2.8 | DESI MSI data pre-processing

Raw DESI MSI data were pre-processed using a pipeline reported by Inglese et al. (Inglese et al., 2021). Briefly, a Kneedle (Satopaa et al., 2011) algorithm-based modification of the method of Zhurov et al. (Zhurov et al., 2014) was applied to separate baseline noise from sample-related signals, followed by a further smoothing procedure using Savitzky–Golay filter (degree = 3, window = 11) to remove the sample-dependent noise. The denoised data were then used for peak detection, with centroid mass/charge (m/z) values assigned to peaks and the highest raw intensities within the base points interval retained as the peak intensity values. To allow the identification of tissue-related pixels, intra-run peaks were first recalibrated using a single lock mass m/z 255.233 and m/z 309.2306 as reference peaks in the negative and positive modes, respectively. The choice was based on the observation that these ions were detected in both tissue and off-tissue pixels. A linear support vector machine classifier trained on manually annotated pixels was used to predict the tissue region-of-interest (ROI) pixels. SPUTNIK spatial filtering was therefore applied to filter out tissue-unrelated peaks. Peaks with a positive Pearson's correlation with ROI or those that were not statistically different between the regions inside and outside the ROI ($p < 0.05$, t-test without multiple testing correction was applied as a conservative approach) were considered non-tissue related and then removed. (Inglese et al., 2019) All non-tissue pixels were removed from the dataset, subsequently to the peak filtering. Thereafter, masses were recalibrated using the method described in (Ramesh et al., 2018). Intra-run peak matching was performed using MALDIquant 'relaxed' method with a tolerance of 50 ppm (Gibb & Strimmer, 2012). Representative peak lists were used to perform inter-run peak matching. A peak list consisting of the intra-run matched m/z values and their mean intensity calculated over the ROI pixels was used as a representative for each run for inter-run peak matching. Inter-run peak matching was performed using the MALDIquant 'relaxed' method with a tolerance of 20 ppm. Only inter-run-matched m/z values with a mean intensity different from zero in all runs were preserved, and all other peaks were discarded. Finally, feature matrices corresponding to the inter-run-matched m/z intensities of ROI pixels were generated, assigning the intensities of the original peaks. All DESI MSI raw data are available on METASPACE (https://metaspace2020.eu/).

2.9 | Network analysis

Using pre-processed data, a weighted graph was constructed based on the shared nearest neighbors between nodes. (Zhu et al., 2020) As a first step, in order to avoid a bias in the image similarity because

of artifactually high signal in the tissue borders, pixels of the ROI borders were removed using a diamond kernel of size 3 pixels. The feature matrices were normalized using quantile normalization, followed by feature winsorizing to reduce the effects of outliers. For each feature, signals lower than 0.01 quantile and higher than 0.99 quantile were assigned to the selected thresholds, respectively. Because of the presence of multiple samples and biological replicates, we constructed a consensus graph from all samples belonging to the same genotype. For each run, Spearman's correlations between all ion intensities were calculated, representing the similarity between their spatial distributions (images). Based on this similarity, the graph adjacency matrix was calculated as the shared 20-nearest-neighbors between each pair of ions and pruning the values smaller than 1/15, using the Seurat package for R. (Satija et al., 2015) Adjacencies corresponding to the biological replicates were merged by taking the mean value of each matrix element. The final consensus adjacency matrix, corresponding to the samples of the same genotype, was calculated, assigning to each element the minimum value across the three adjacencies.

For community detection, a dendrogram calculated using the consensus adjacency as distance (linkage = average) was partitioned using the Dynamic Tree Cut method with the smallest module size equal to five. (Langfelder et al., 2008) This choice assumed that at least one or two ions with their ^{13}C isotopes would be assigned to a module. Module eigenmetabolites (ME) were calculated as representative spatial distributions of each graph module. (Langfelder & Horvath, 2007) ME values corresponded to the first principal component scores of the run feature matrix, using only module features. If Pearson's correlation between ME values and the pixel-wise mean signal was negative, the ME values signal was reversed. ME were plotted as images to visually identify the possible spatial patterns associated with each module. For ease of representation, each DESI ion image was scaled independently to provide similar global color scale contrasts.

2.10 | Comparison between brain regions

Brain regions corresponding to the hippocampus and cortex were manually annotated using VIA software. (Dutta & Zisserman, 2019) Mean intensities of selected features were calculated from the annotated regions and tested for the statistical difference by three mixed-effect linear models, one for each genotype:

$$y_{ij} = \beta_0 + \beta_g x_{ig} + \beta_b x_{ib} + \beta_m x_{ig} x_{ib} + u_j + \varepsilon_{ij},$$

where y_{ij} represents the mean intensity of the median normalized ion (assumed to be normally distributed, and the normality was checked with quantile-quantile plot) of the i-th pixel in the j-th run, x_{ig} is the binary predictor associated with the brain region, and u_j is the random intercept of the j-th run. The models were fitted using 'nlme' R package. (Pinheiro et al., 2017) The significance of non-zero fixed effect coefficients of all pair-wise comparisons (region, genotype) was tested using the 'emmeans' R package ($p < 0.05$, Tukey's correction). (Lenth, 2021)

2.11 | Reversed phase LC–MS profiling of brain tissue lipidome

Tissues were extracted using the Folch method (Folch et al., 1957). Briefly, 1× Halt Protease and Phosphatase Inhibitor Cocktail (Thermo Scientific) was dissolved in a MeOH/CHCl3 (1:2) mixture to make the extraction solution and kept at −20°C overnight. Then, frozen tissues were mechanically homogenized in a cold extraction solution using ceramic beads. The organic phases were combined and dried under gentle nitrogen flow at room temperature. The samples were reconstituted by adding 75 μL of 1:4 H_2O:Isopropanol containing standard mix (LPC(9:0/0:0); PC(11:0/11:0); FA(17:0); PE(15:0/15:0); PA(17:0/17:0); PG(15:0/15:0); PS(17:0/17:0); Cer(d18:1/17:0); DG(19:0/0:0/19:0); PC(23:0/23:0); TG(15:0/15:0/15:0); TG(17:0/17:0/17:0)), vortexed for 1 min, sonicated for 10 min, put on an orbital shaker for 10 min at 3896 g at 4°C. These standards are not isotopically labeled and are used for analytical quality control only. Samples were individually vortexed until complete pellets were dissolved. The samples were centrifuged for 10 min at 3896*g* at 4°C. A quality control study reference sample (SR) was generated by pooling 35 μL from each sample. For each sample, 25 μL was transferred into an Eppendorf, and 25 μL of 1:4 H_2O: IPA containing the standard mix was added. The samples were vortexed for 5 s and then put on an orbital shaker for 5 min at 3896 g at 4°C. The samples were then centrifuged for 1 min at 3986*g* at 4°C. 24 μL was transferred to a vial for each polarity. SR runs between samples were prepared the same way. From each vial, two μL and one μL of the sample were injected for negative and positive polarity, respectively, onto a Waters Acquity UPLC BEH C8, 1.7 μm, 2.1 × 100 mm column (Waters Corp.) kept at 55°C using an ACQUITY UPLC system (Waters Corp.). The mobile phase consisted of water:isopropanol: acetonitrile (2:1:1, all high-grade LC–MS solvents from Fisher Scientific or Sigma-Aldrich), 5 mM ammonium acetate, 0.05% acetic acid, 20 μM phosphoric acid (A) and isopropanol: acetonitrile 1:1 (Sigma-Aldrich), 5 mM ammonium acetate, 0.05% acetic acid (B). Each sample was resolved for 13.15 min at a 0.6 mL/min flow rate. Starting conditions were 99% A and 1% B. The gradient changed with a ramp of curve 6 as follows: decrease to 70% A and 30% B over the first 2 min, decrease to 10% A with 90% B from 2 to 11.50 min, decrease to 0.1% A with 99.9% B from 11.50 to 12 min while increasing the flow rate to 1 mL/min, staying at 99.9% B for 0.5 min, after which the solvent composition returned to starting conditions over 0.25 min until 13.15 min. MS was performed on a Xevo G2-S oaTOF MS (Waters Corp., Manchester, UK) coupled to the UPLC via a Zspray electrospray ionization (ESI) source. The capillary voltage was set to 1.5 kV for negative polarity and 2 kV for positive polarity, the sampling cone voltage to 25 V, and the source offset equal to 80 V. The StepWave 2 offset to 15 V. The desolvation gas flow was set to 1000 L/h, the desolvation temperature to 600°C, with a cone gas flow of 150 L/h and a source temperature of 120°C. Accurate mass was maintained by introduction of LockSpray interface of Leucine Enkephalin (m/z

278.1141 and 556.2771 in ESI+, m/z 236.1035, and 554.2615 in ESI−) at a concentration of 600 pg/μL in 50% aqueous acetonitrile with a scan time of 0.15 s over 4 scans, after each interval of 60 s. Data were collected in centroid mode from 50 to 2000 m/z in MS scanning mode. The SR was also used to condition the column (30 injections), followed by a dilution series of the SR sample to allow data filtering. To ensure system stability and data normalization, the SR sample was injected at regular intervals throughout the analytical run (Izzi-Engbeaya et al., 2018; Lewis et al., 2022).

2.12 | LC–MS data analysis

The raw LC–MS data were converted to mzML (Deutsch, 2010) using Proteowizard msconvert (Chambers et al., 2012), removing all centroids with intensity lower than 100. Peak detection was performed using R (v4.0.1) package XCMS (Smith et al., 2006; v3.10.0) and the centWave algorithm with the following parameters: ppm = 25, peakWidth = (3, 12), mzdiff = 0.001, pre-filter = (4, 1000), noise = 600, and snthresh = 5. Features were grouped with the 'density' method, with parameters bw = 3, mzwid = 0.0007, and minFrac = 0.4. Intensities from non-detected signals were numerically integrated using the 'fillPeaks' method with default parameters. No retention time correction was applied. The Python (v3.9.0) library 'nPYc-Toolbox' (v1.2.5; Sands et al., 2019) was used to correct for run-order intensity drifts using a LOWESS trendline estimated on repeated injections of the pooled study reference sample (Cleveland & Devlin, 1988), filter features with a Pearson correlation between intensity in SR serial dilution and dilution factor less than 0.7, and with a coefficient of variation estimated from the repeated injections of the SR sample of less than 30%. Intensities were normalized with probabilistic quotient normalization (Dieterle et al., 2006) to account for differences in tissue weight and extraction efficiency, with the median spectra chosen as a reference. Metabolic differences between mouse lines were determined using a linear mixed effect model with the formula log(Metabolite +1) ~ mouse line + (1|Mouse). The mouse line was modeled as a fixed effect and a random intercept per individual mouse. These analyses were performed with the "lme4" (Bates, 2010; v1.1.25) and "emmeans" (Lenth et al., 2019; v1.2.5.1) packages. P-values were calculated using the Satterthwaite approximation for degrees of freedom estimated and Storey's q-value procedure implemented in R package qvalue (Storey et al., 2015) (v2.20.0) for false discovery rate correction. Figures were generated with ggplot2 (Wickham, 2011) (v3.3.3). All raw LC–MS data are publicly available on the Metabolights repository (https://www.ebi.ac.uk/metabolights/MTBLS551/) (Lewis et al., 2022).

3 | RESULTS

3.1 | Age-related changes in Aβ immunostaining and associated cellular pathology in the brains of App$^{NL\text{-}G\text{-}F}$ and h-Aβ mice

We first characterized brain Aβ plaque formation and glial activation in the 2.5-, 7-, and 12-month-old App$^{NL\text{-}G\text{-}F}$ and WT mice to be used for mass spectrometry imaging (MSI). We localized Aβ using mOC87 (Figure 1a) and 6C3 antibodies (Figure 1a–c; Hatami et al., 2014). Positive immunostaining for Aβ was detected in cortical regions of App$^{NL\text{-}G\text{-}F}$ mice as early as 2.5 months, consistent with previous findings (Saito et al., 2014). Immunostaining with the mOC87 antibody revealed fewer, smaller plaques (2.5 months, 25–100 μm; 12 months, 50–250 μm) with a less dense appearance in younger compared to older mice (Figure 1b,c). There was an age-dependent increase in App$^{NL\text{-}G\text{-}F}$ mice not observed in WT mice, with a 2-fold higher GFAP+ cell density at 12 months compared to 2.5 months of age ($p = 0.0065$; Figure 1c). The density of CD68^{+} microglial cells increased 20- ($p = 0.0099$) and 90-fold ($p = 0.0001$) in 7- and 12-month-old App$^{NL\text{-}G\text{-}F}$ mice, respectively, relative to WT. Similar relative glial changes were found in cortical (Figure 1c) and hippocampal (Figure S1) sections. We observed diffuse 6C3+ immunostaining in the hippocampus and cortex of h-Aβ mice (Figure 1d) but did not identify plaque-like aggregates or find evidence for increased CD68+ or GFAP+ cell densities relative to WT.

3.2 | Spatially resolved lipidomics with DESI MSI identifies punctate patterns of lipid co-expression with Aβ plaques in App$^{NL\text{-}G\text{-}F}$ mice

We then employed DESI MSI to distinguish lipidomic differences in the App$^{NL\text{-}G\text{-}F}$ model relative to WT. Similar observations in the h-Aβ model allowed the potential differences in lipid composition

FIGURE 1 Age-related changes in Aβ aggregates and cellular pathology in the brains of App$^{NL\text{-}G\text{-}F}$ and h-Aβ mice. (a) Immunostaining with the mOC87 (or 6C3 in c, d, relative ratio by area) antibody reveals Aβ aggregates in the left hemisphere of a 12-month-old App$^{NL\text{-}G\text{-}F}$ mouse brain, highlighting the punctate distribution of larger plaques across diverse brain regions. An anatomical map of the right hemisphere (adapted from P56, coronal, mouse brain, Allen Brain Atlas, Available from atlas.brain-map.org) provides an anatomical reference. (b) Enlarged view of mOC87-stained amyloid plaques in 2.5-, 7-, and 12-month-old App$^{NL\text{-}G\text{-}F}$ mice demonstrate smaller and less diffuse Aβ aggregates at 2.5 months, evolving into more prominent and diffuse plaques in 7- and 12-month-old mice. (c) Comparative analysis of staining patterns for three markers (6C3, GFAP, and CD68) in cortical regions ($n = 3$, 2-way ANOVA, Tukey, 95% confidence interval, DF = 12, columns show mean ± SEM. The complete multiple comparisons report can be found in the supplementary file) between App$^{NL\text{-}G\text{-}F}$ and wild-type (WT) mice illustrates an age-dependent increase in Aβ burden, coinciding with astrocytic and microglial activation. Representative staining for each marker in App$^{NL\text{-}G\text{-}F}$ and WT is provided. (d) 6C3 antibody staining in sections of 12-month-old WT and h-Aβ mice indicates diffuse positive reactivity in the hippocampus and cortex of h-Aβ mutants, contrasting with the absence of such reactivity in WT mice.

Journal of Neurochemistry JNC The Official Journal of the International Society for Neurochemistry WILEY

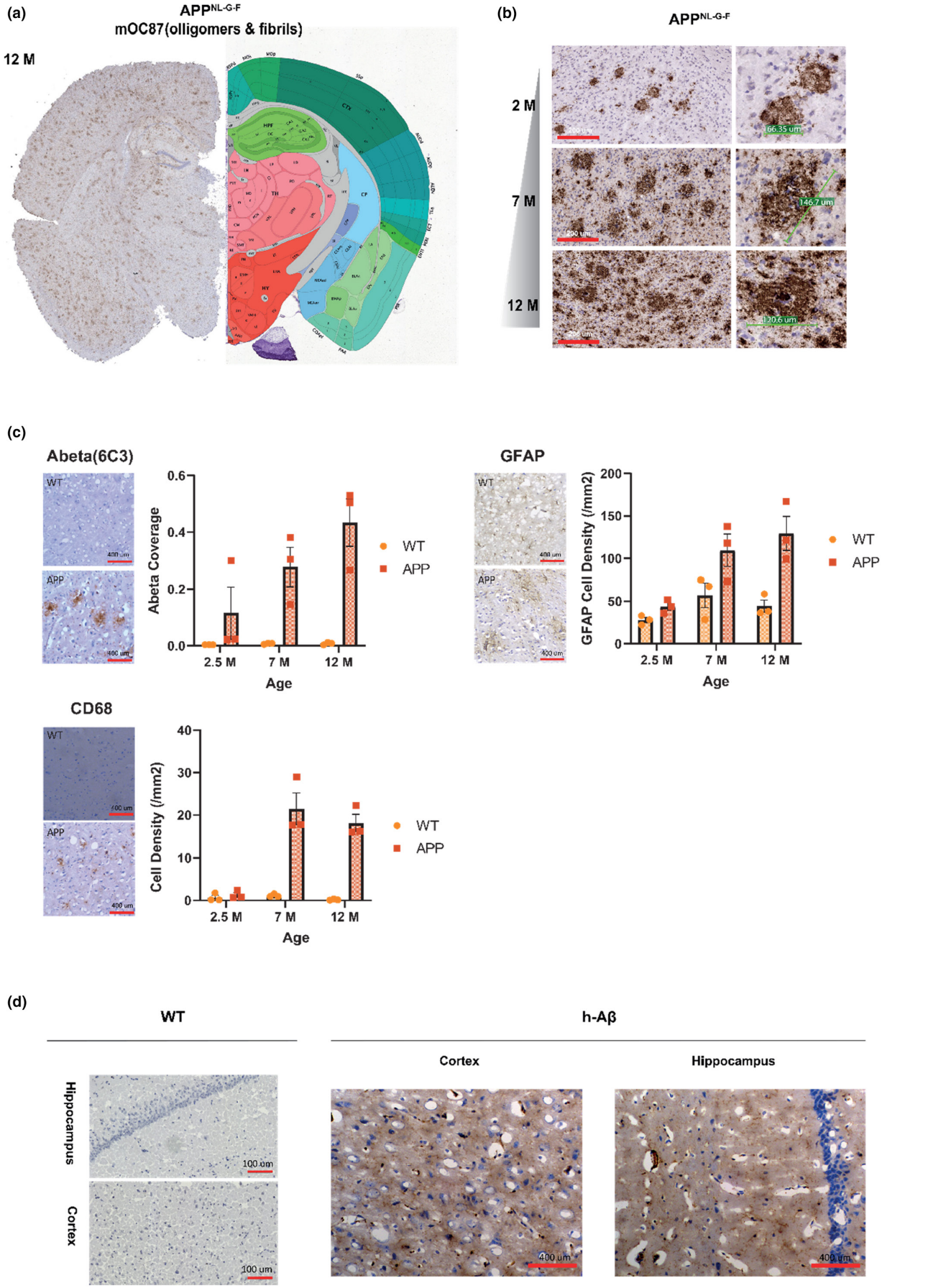

with expression of human *APP* to be explored. MSI was initially performed on whole tissue sections from 12-month-old App$^{NL\text{-}G\text{-}F}$, h-Aβ, and WT mice at a notional linear resolution of 75 μm. To identify differences in distributions of lipids between these mice, we generated a shared nearest neighbor graph-based consensus network (Zhu et al., 2020) to describe patterns of spatial co-expression of lipids (Figure 2a). Assuming that biologically related molecules have similar distributions in tissues (Inglese et al., 2018), we can interpret the spatially defined graph modules of co-expressed lipids in these networks in terms of their potential functional biological relationships.

The spatial lipidome co-expression graphs' networks obtained from DESI MSI of the App$^{NL\text{-}G\text{-}F}$ brain sections included 16 and 23 modules in the positive and negative DESI MSI modes, respectively (Figure 2b, eigen images and top 10 module ions for negative mode can be found in Table S2, and the positive mode in Table S3). These MSI graphs highlighted the regional heterogeneity in lipid composition expected as a consequence of differences in regional cell composition and metabolism (Figure 2c; Fitzner et al., 2020). However, distinct spatial distributions of the Cyan module in the positive mode and the Sienna3 module in the negative mode (Figure 2d) also distinguished the App$^{NL\text{-}G\text{-}F}$ mice from both h-Aβ and WT mice. Both modules predominantly localized to the hippocampal and cortical gray matter in the three mouse models, but they uniquely showed a multifocal, punctate distribution in the App$^{NL\text{-}G\text{-}F}$ mouse (Figure 2d). Assignments for the individual ions in the positive acquisition mode based on m/z values suggested that the positive mode Cyan module was enriched in palmityl and stearyl lysophosphatidylcholines (LPCs) and lysophosphatidic acids (LPAs; Figure 2c). We also observed a narrow band of expression along the external wall of the latter ventricles in some mice. Negative mode Sienna3 module expression was associated with the hippocampi and pyramidal and granular cell layers in all three mouse models but showed multifocal punctate increases only in the App$^{NL\text{-}G\text{-}F}$ mice. This module included bis(monoacylglycerol) phosphates (BMPs), polyunsaturated phosphatidylglycerols (PGs), lysophosphatidylglycerols (LPGs), and lysophosphatidylinositols (LPIs; Figure 2c,d; Table S4).

To validate our annotations of the DESI MSI features of interest, we performed in situ MS/MS experiments (Figure S2). These confirmed the fragmentation patterns characteristic of potassiated and sodiated forms of lysophospholipids associated with the positive mode Cyan module (Domingues et al., 2001; Wang et al., 2010). The lysophospholipids (LPLs) fragmentation patterns in the positive mode were also confirmed, distinguishing them from isomeric lyso-PAF (Anderson et al., 2017; Gazos-Lopes et al., 2014). Assignment of BMPs in the negative mode Sienna3 module was consistent with previously reported MS/MS fragmentation (Anderson et al., 2017; Nielsen et al., 2016).

The punctate distribution of LPLs, PGs, and BMPs in brain sections from App$^{NL\text{-}G\text{-}F}$ mice suggested co-localization with Aβ plaques. To test this, we immunostained tissue sections with the amyloid fibril antibody-sensitive mOC87 after DESI acquisitions at 75 μm (Figure S3) and 25 μm (Figure 3a) resolutions. The punctate patterns of lipids in the Cyan and Sienna models in App$^{NL\text{-}G\text{-}F}$ mice co-localized with Aβ plaques. We, therefore, will refer to these lipid modules identified through positive or negative mode DESI MSI in App$^{NL\text{-}G\text{-}F}$ mice as plaque-enriched module (PEM).

3.3 | Differences in associations of PEM lipids and glial cell activation markers highlight the heterogeneity of plaques in App$^{NL\text{-}G\text{-}F}$ mouse brains

The relative co-localization of PEM lipids with Aβ plaques in the App$^{NL\text{-}G\text{-}F}$ model increased with age. LPC (18:0) enrichment at 25 μm resolution was co-localized with ca. 5% of 50–300-μm diameter Aβ plaques in 2.5-month-old mice. At 7 months, LPC (18:0) enrichment co-localized with ca. 42% of plaques, and at 12 months focal LPC (18:0) puncta co-localized with approximately ca. 70% of plaques (Figure 3b). We also found that Aβ plaques were more frequently associated with PEM LPCs and lysophosphatidic acids (LPAs) (positive mode) in 12-month-old App$^{NL\text{-}G\text{-}F}$ mice than at younger ages (Figure 3b). Similar trends were observed for negative mode PEM lipid features. Accumulation of BMP (44:12), polyunsaturated PGs, and LPIs around Aβ plaques also was less common at 2.5 months (with BMP (44:12) enrichment co-localized with 3% of plaques) and 7 months (with BMP (44:12) enrichment co-localized with 26% of plaques) compared to 12 months of age (with BMP (44:12) enrichment co-localized with 65% of plaques). These findings were supported by an age-dependent increase in the total extractable levels of LPC (18:0) and BMP (44:12) and other PEM lipids in the brains of homozygous and heterozygous App$^{NL\text{-}G\text{-}F}$ mice (n = 6) (Figure 3c).

Lipids such as LPCs and LPAs identified in PEMs can potentiate or modulate glial inflammatory responses in the case of BMP, a regulatory lipid influencing lysosomal integrity and function. In the 2.5-month-old animals, approximately 5% of Aβ plaque co-localized with CD68^{+} microglia (by area). Co-localization analyses showed that immunoreactivity for the lysosomal marker, LAMP1, was found in about 20% of areas in and around Aβ plaques (Figure 4a,b). In the 7-month-old App$^{NL\text{-}G\text{-}F}$ mice, 30% of mOC87+ plaques were co-localized with LAMP1, and 20% of these were CD68^{+}. The highest LAMP1 expression was observed in and around some of the larger plaques (especially in the cortex) (Figure 4a), consistent with lysosomal activation in the evolution of plaques from early to late morphologies (Dickson & Vickers, 2001). By 12 months of age, most cortical plaques were associated with CD68+ microglia and focally enriched with PEM LPCs (Figure 5a–d). GFAP+ astrocytes co-localized with 75% of mOC87+ plaques (Figure 5e–h). CD68+ and LAMP1+ reactivities also were frequent in the dentate polymorphic cell layer along with particularly high focal concentrations of BMP (44:12). Finally, DESI MSI also showed relative focal depletion of sphingomyelin (SM) (d36:1) and several hexosylceramides (HexCers) (identified by m/z values and validated by in situ MS/MS) around plaques relative to the normal-appearing gray matter. This

Journal of Neurochemistry JNC The Official Journal of the International Society for Neurochemistry WILEY

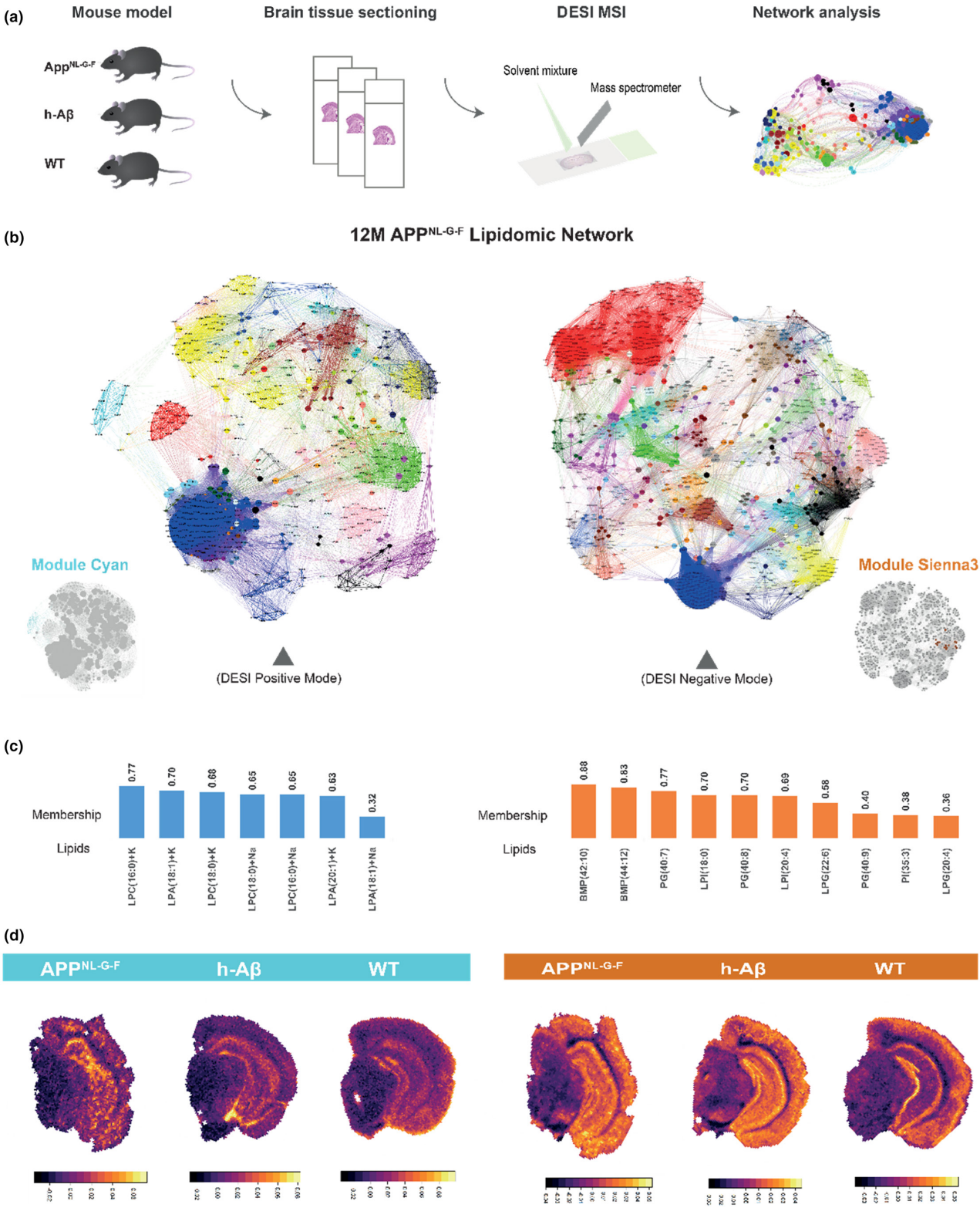

FIGURE 2 Spatially resolved lipidomics with DESI MSI identify multifocal accumulations of specific lipids in App$^{NL\text{-}G\text{-}F}$ mice. (a) Schematic overview of the DESI tissue analysis methodology employed in this study. (b) Consensus shared nearest neighbor graph networks were constructed from 12-month-old App$^{NL\text{-}G\text{-}F}$ mouse coronal sections ($n = 6$, 3 females and three males), acquired at a 75-μm resolution using positive and negative DESI modes. The Cyan and Sienna3 modules are prominently highlighted, depicting intricate and strong inter-lipid associations. (c) Constituent lipids of the highlighted Cyan and Sienna3 modules are presented, ranked by their module membership values. Ion assignments are based on accurate mass values using the Metlin database, with corresponding mass errors detailed in Table S1. (d) The eigen images of Cyan and Sienna3 module ions exhibit punctate distributions within App$^{NL\text{-}G\text{-}F}$ mouse brain sections. In contrast, brain sections from h-Aβ and WT mice display distinct, diffuse, and regionally variable distributions of these ions.

likely reflects myelin and synaptic loss in and around these plaques (Kaya et al., 2020; Figure S4). These results together describe the evolution of the cellular and lipid pathology in and around plaques as they age. DESI MSI highlights that lipidomic evidence for myelin and synaptic injury is most significant in the later stages of plaque evolution when most plaques are associated with activated microglia (Depp et al., 2023).

3.4 | Differences in the cortical lipidome distinguish h-Aβ and WT mice

h-Aβ mice exhibit diffuse mOC87+ Aβ protofibrils in the cortex and do not display signs of microglial activation but, as described here, show morphological changes (hypertrophy and retraction of processes) consistent with astrocyte activation (Baglietto-Vargas et al., 2021). We explored whether h-Aβ also expresses PEM lipids in a spatial pattern, distinguishing them from the WT mice. We found a negative mode Green module unique to the h-Aβ mice that expressed phosphatidic acid (PA) (38:6) and lysophosphatidic acid (LPA) (22:6; Figure 6a), providing evidence for increased autotaxin-LPA signaling (Ramesh et al., 2018) and mild inflammatory pathology with astrocyte and phospholipase D activation (generating PA; Oliveira & Di Paolo, 2010) with the expression of Aβ fibrils in h-Aβ mice. Other PEMs had different neuroanatomical distributions in the WT and h-Aβ cortical tissues (Figure 6b). For example, the hippocampus of h-Aβ mice had higher expression of LPA (20:1) and two LPCs compared to the cortex (Figure 6c; Figure S5). BMP (44:12) was singularly enriched in the h-Aβ mouse hippocampus but showed similar expression levels in both the cortex and hippocampus of WT mice. Inositol cyclic phosphate and LPIs contributing to the WT Magenta module were not expressed in the corresponding modules in the h-Aβ mice.

In contrast, negative mode PEM lipids were represented in comparably spatially distributed co-expression modules in the h-Aβ and WT mice across two modules distributed spatially in a similar fashion in both WT (Darkorange2 and Magenta modules) and h-Aβ (Lightyellow and Green modules) mice (Figure 6a,b, with the complete ion list of these modules in Table S5). In the h-Aβ Lightyellow module and the WT Darkorange2 module, LPG (22:6) co-localized with two other DHA-containing BMPs (BMP (22:6/22:6) and BMP (22:6/20:4)) and with polyunsaturated PGs. Lipids, including LPI (20:4) and LPI (18:0), were co-localized with other LPLs (e.g., LPAs, lysophosphatidylethanolamine(LPEs)) and precursor phosphoinositides (PIs) and fatty acids, including stearic and palmitic acids both in the h-Aβ Green module and in the WT Magenta module.

3.5 | DESI MSI defines lipidomic differences not apparent from LC–MS analysis of bulk cortical tissue extracts

We investigated the added value of spatially resolved lipid profiling by comparing the differences identified above between WT, h-Aβ, and App$^{NL\text{-}G\text{-}F}$ mice with those apparent from LC–MS bulk lipidomic analyses. Principal component analysis of the bulk lipid extracts revealed distinct lipid clusters corresponding to each genotype (Figure 7a). Linear mixed effect models identified FA (20:3), LPI (18:0), LPI (20:4), and several HexCers as the most discriminant features distinguishing the mice (Table S6). We then explored amounts of the total extractable PEM lipids ($n=3$). Consistent with identifying PG as a PEM negative mode lipid, PG concentrations were highest in the App$^{NL\text{-}G\text{-}F}$ mouse brains, followed by h-Aβ and WT mice (Figure S6). App$^{NL\text{-}G\text{-}F}$ and h-Aβ brain lipid extracts had higher concentrations of lysophospholipids (LPLs) and BMP (44:12) compared to the WT group, but we did not find differences in the amounts in lipid extracts from h-Aβ and App$^{NL\text{-}G\text{-}F}$ mice (Figure 7b). By identifying the same chemical species, these observations validate the DESI MSI. They also underscore the independent contribution made by spatially resolved lipid profiling for discriminating lipid pathology, which is not evident from traditional bulk tissue analyses when sample size is relatively small.

3.6 | AD brains show PEM lipid expression co-localized to Aβ plaques

To test whether related lipids are co-expressed with Aβ plaques with AD, we performed DESI MSI (25 μm resolution) on human brain sections from the entorhinal cortex and middle temporal gyrus of non-diseased control (Braak Stage 0 to 2, $n=8$) and AD (Braak Stage 5 to 6, $n=7$) donors obtained (Table S7). The non-disease controls have a mean density of only 40% as many Aβ plaques as AD brain sections ($p=0.0327$) (Figure 8a). We constructed molecular co-localization networks using the same pipeline as the mouse datasets. For DESI positive mode, we identified 223 lipid co-expression modules in AD brain sections, from which four modules showed focal lipid puncta spatially associated with Aβ plaques (Figure 8b,c; Table S8). Module 80 was expressed in gray matter and included predominantly sodiated forms of LPA (18:1), LPC (18:0), and LPC (16:0). Modules 31 and 51 were expressed in both gray and white matter (Iwamoto et al., 1997). Module 31 contained potassiated adducts of LPAs and LPCs and two HexCers (34:1;O2, 36:2;O2). Module 51 included a different group of LPCs, including LPC (20:4, 22:6, 20:3, 16:1). The differences in PEM lysophospholipids suggest activation of different sub-types of phospholipase A2 (PLA2) (Sun et al., 2021). Module 74 involved primarily local co-expression of a group of ceramides (Figure 8b). Interestingly, module 31 HexCers were more co-expressed but did not show obvious focal localization with Aβ plaques. As a matter of fact, in the AD group, HexCer(d42:2) and other HexCer in module 2 (Figure S7a) were relatively reduced in the LPC-enriched puncta associated with plaques (Figure S7b), likely reflecting local loss or dystrophy of myelinated axons (Kirilina et al., 2020; Roussarie et al., 2020).

DESI-MSI of cortical tissues from non-diseased control donors generated a different lipidomic network. Fewer modules were

Journal of Neurochemistry JNC The Official Journal of the International Society for Neurochemistry WILEY

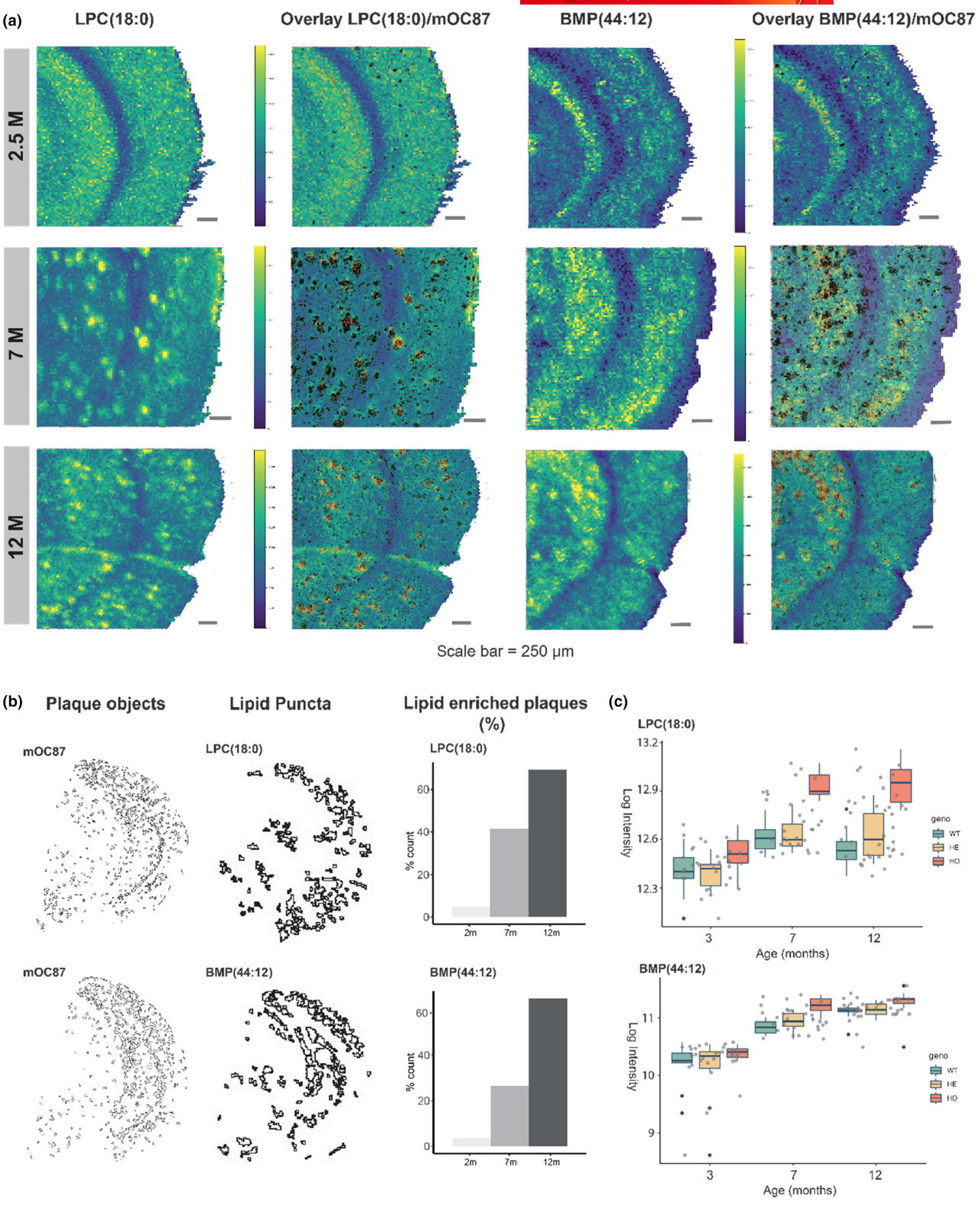

FIGURE 3 Positive and negative mode lipid modules identified in the App$^{NL\text{-}G\text{-}F}$ mice co-localize with Aβ plaques. (a) DESI ion images of two representative lipids (LPC (18:0) and BMP (44:12)) from the Cyan and Sienna3 modules, respectively, are superimposed onto amyloid plaques stained with mOC87 antibody. Images are captured from hippocampal and cortical regions of 2.5-, 7-, and 12-month-old APP$^{NL\text{-}G\text{-}F}$ mice. DESI MSI data were acquired at a high resolution of 25 µm. (b) Larger plaques (50–200 µm) and yellow punctate signals of LPC (18:0) and BMP (44:12) lipids were quantified and exemplified in one 12-month-old brain. Proportions of lipid-enriched plaques are displayed for all three age groups in App$^{NL\text{-}G\text{-}F}$ mice, demonstrating an age-dependent increase. (c) We also performed quantification of the total levels of these lipids in extraction-based LCMS analysis, and age-dependent increase were shown in the homozygous App$^{NL\text{-}G\text{-}F}$ mice when compared to heterozygous and wild-type littermates.

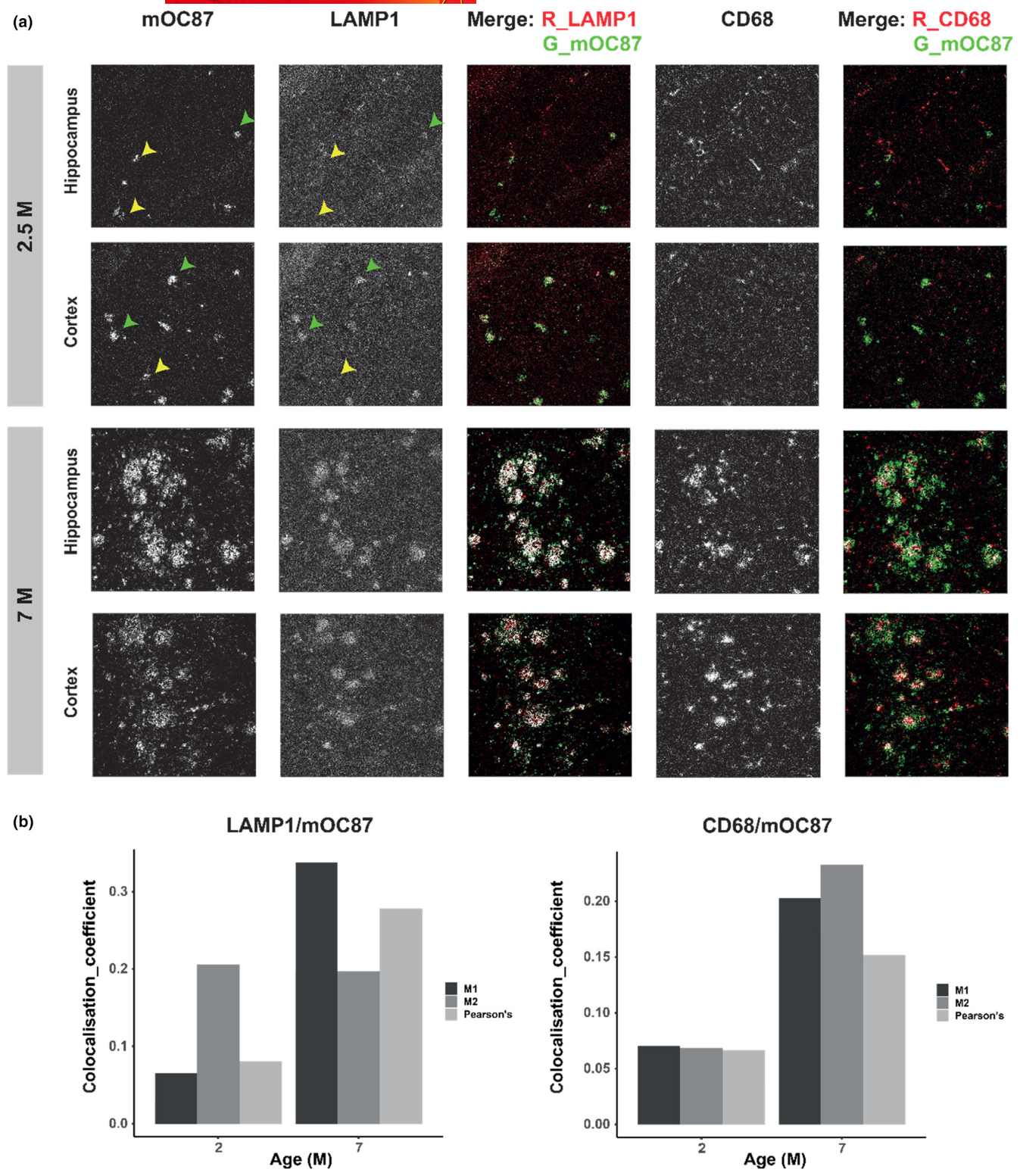

FIGURE 4 Differences in associations between glial activation markers highlight the heterogeneity of Aβ plaques in the App^{NL-G-F} mice. (a) Co-localization analysis of mOC87, CD68, and LAMP1 signals in 2.5- and 7-month-old App^{NL-G-F} mice was performed. In 2.5-month-old animals, LAMP1−mOC87+ plaques are indicated by yellow arrows, while a green arrow highlights LAMP1+ mOC87+ plaques. No CD68+ mOC87+ plaques were observed at 2.5 months. However, at 7 months, many plaques exhibited co-localization of LAMP1, mOC87, and CD68 signals. (b) Quantification of co-localization coefficients (Pearson's, M1, M2) was conducted to assess the degree of co-localization between amyloid and LAMP1 or CD68 signals using Imaging Mass Cytometry. Co-localization coefficients were determined through the application of JACOP (Bolte & Cordelieres, 2006) in Fiji. Notably, 7-month-old animals demonstrated elevated co-localization coefficients. M1 represents the proportion of the LAMP1 or CD68 area that co-localizes with the Aβ area, while M2 signifies the ratio of the Aβ area that co-localizes with the LAMP1 or CD68 area.

Journal of Neurochemistry JNC The Official Journal of the International Society for Neurochemistry WILEY

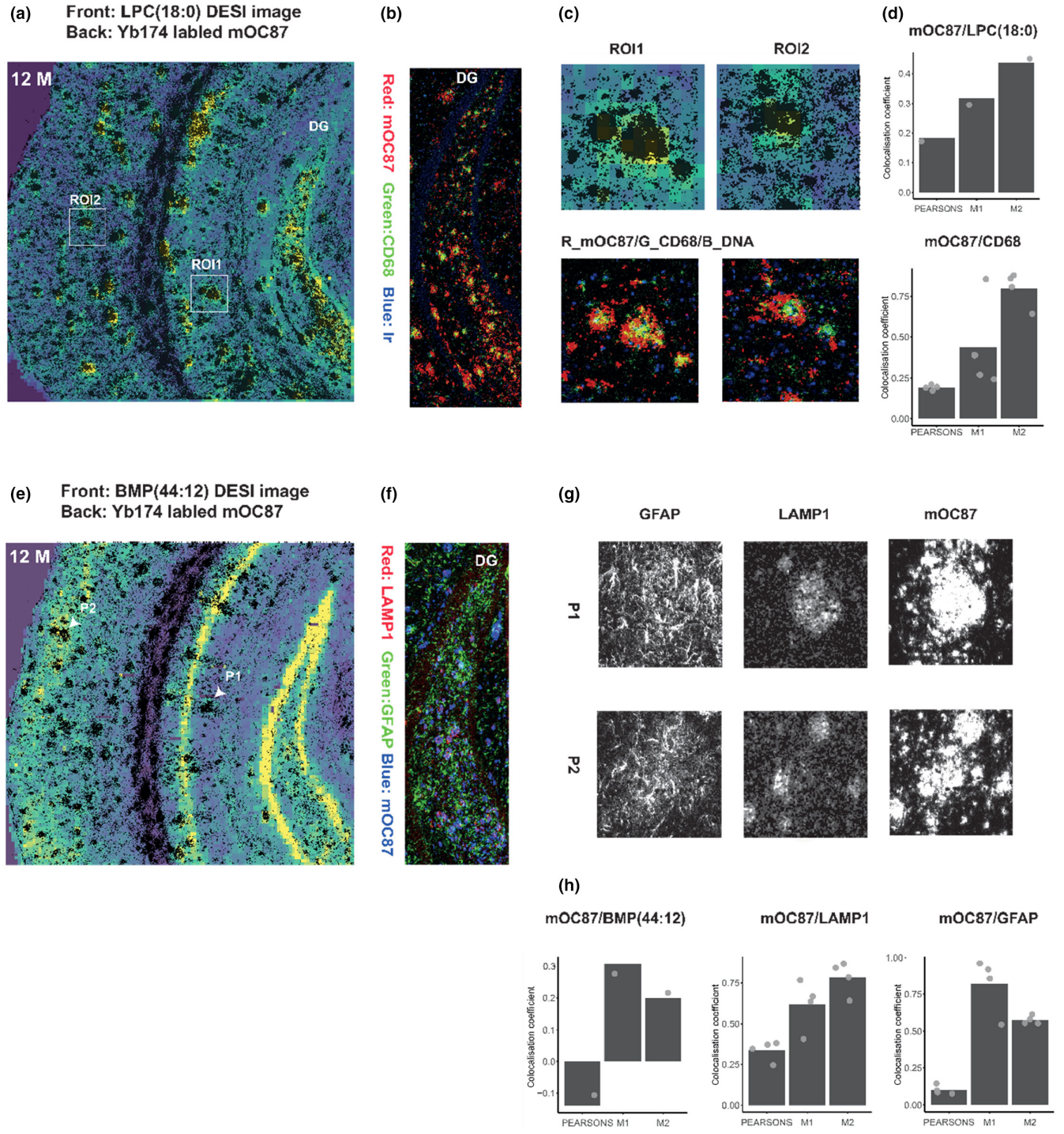

FIGURE 5 Co-registration of lipid plaque markers identified in DESI and IMC markers in a 12-month-old App$^{NL\text{-}G\text{-}F}$ mouse. (a) Overlay of the LPC (18:0) signal with Yb174-labeled mOC87 staining acquired from imaging mass cytometry, featuring two regions of interest (ROIs) for analysis. (b) Enlarged view of a dentate gyrus region highlighting the accumulation of CD68+ pre-plaque forms co-localizing with a high level of LPC (18:0) signal. (c) Enlarged view of mOC87 and CD68 staining within the described ROIs (ROI1 and ROI2) from (a). (d) Quantification of co-localization reveals a significant proportion of CD68 (75%) co-localizing with amyloid, along with 40% of LPC (18:0) signal co-localizing with amyloid at 12 months. (e) Overlay of lipid BMP (44:12) signal with Yb174-labeled mOC87 IMC imaging of a section from an App$^{NL\text{-}G\text{-}F}$ mouse, highlighting two plaque regions. (f) Enlarged view of a dentate gyrus region displaying co-localization of lysosomal and astrocytic markers with pre-plaque forms. (g) Depiction of LAMP1, GFAP, and mOC87 expression, revealing astrocyte activation within plaques P1 and P2 from (e). (h) Quantitative assessment of co-localization between amyloid and BMP (44:12), LAMP1 and GFAP. Notably, Pearson's correlation score between BMP (44:12) and mOC87 was negative because of the structural role of this lipid in the granule cell layers, as elucidated in (e).

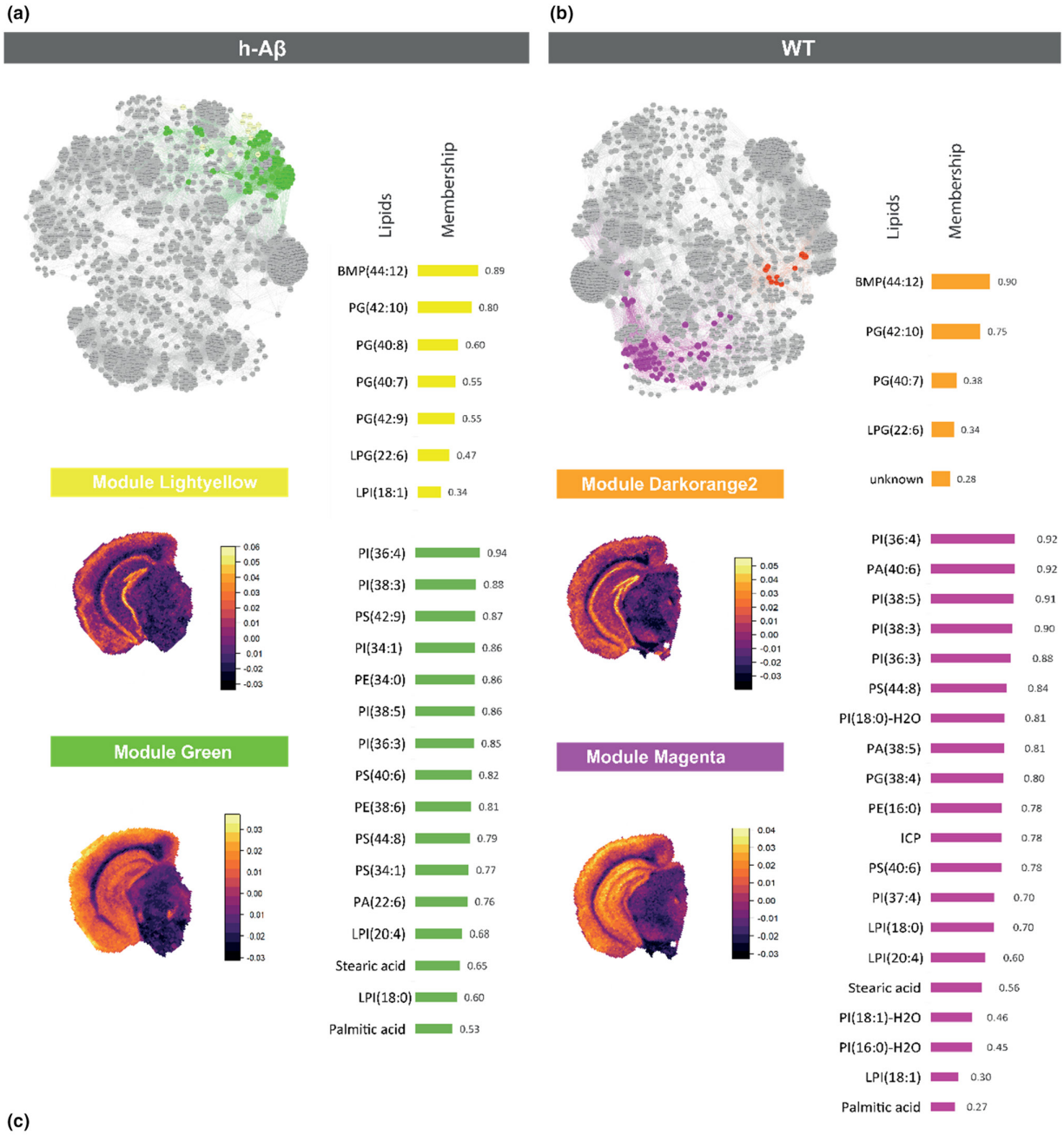

FIGURE 6 Cortical lipidomic changes in h-Aβ mice. (a) A shared nearest neighbor (SNN) network was generated from DESI negative mode imaging data (75 μm resolution) of 12-month-old h-Aβ mice, revealing the module of plaque-associated lipids identified in the App$^{NL\text{-}G\text{-}F}$ mice network were found in two distinct modules (Green and Lightyellow). Major module lipids are listed for reference. These ions are assigned based on the exact mass values through the Metlin Database search. (b) Corresponding SNN networks from 12-month-old WT mice, illustrating modules Darkorgange2 and Magenta linked to the module of plaque-associated lipids identified in the App$^{NL\text{-}G\text{-}F}$ mice network. Major module lipids are enumerated. (c) The DESI imaging data demarcated Hippocampal and cortical regions, and Plaque-enriched module (PEM) lipids were compared between the h-Aβ and WT mouse lines.

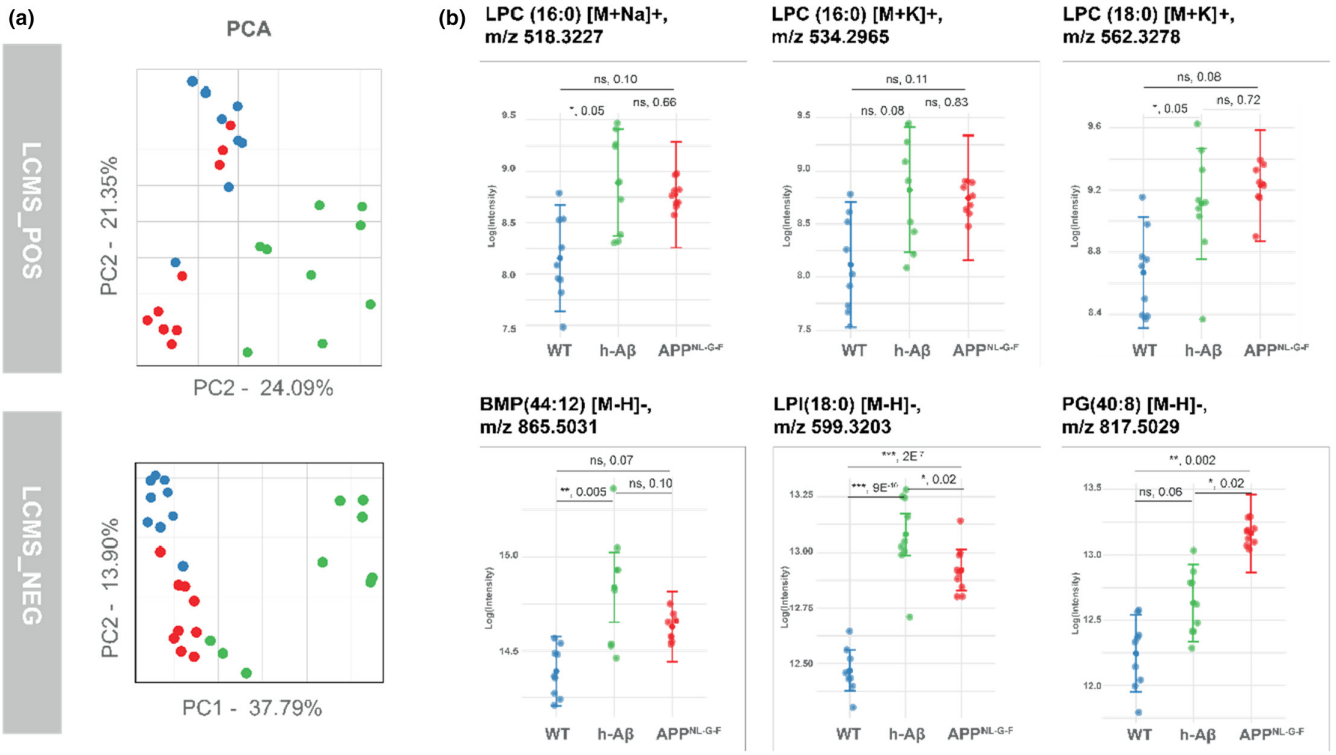

FIGURE 7 DESI MSI reveals nuanced lipidomic disparities not evident through bulk cortical tissue extract LC–MS analysis. (a) Multivariate analysis of LC–MS data in positive (upper) and negative (lower) modes demonstrates distinct separation among 12-month-old h-Aβ, WT, and App$^{NL\text{-}G\text{-}F}$ mice. Notably, discriminative features are detailed in Table S6. For each LCMS sample, 90-μm-thick tissue sections adjacent to the slides used for DESI MSI analysis were collected and homogenized for lipid extraction. (b) Comparative assessment of total quantities of selected plaque enriched module lipids using LC–MS analysis highlights significant variations. Specifically, LPCs and PG (40:8) exhibit notable elevation in the App$^{NL\text{-}G\text{-}F}$ line, whereas BMP (44:12) and LPI (18:0) display pronounced increases in the h-Aβ line.

identified (91 modules). We explored enrichments of these modules with the AD plaque-associated lipids (Figure 8d; Table S9). While one non-disease control donor showed two modules (25 and 50) expressed in a distribution co-localized with Aβ plaques (Figure 8e), most showed no lipid co-expression specific to Aβ plaques. Increases in ceramides around plaques may most specifically distinguish AD PEM (module 74) from non-diseased control PEMs (Figure 8d) (Akyol et al., 2021; Dehghan et al., 2022). We did not find evidence for focal co-localization of negative mode PEM identified in mice with Aβ plaques. BMP (44:12) was distributed diffusely through the cortex in the non-diseased control sections but showed only weak and variable sub-pial expression with AD (Figure S7c). These data from human AD and mouse amyloid models suggest that PEM lipids are variably expressed, perhaps as a function of the stage of evolution of the associated Aβ plaques. For example, BMP (44:12) (and co-expressed lipids) appear to be focally elevated around plaques earlier in their evolution and not persistently expressed at higher levels than the surrounding normal-appearing tissue.

4 | DISCUSSION

We utilized untargeted DESI MSI with correlative IMC immunohistology to compare and contrast spatial patterns of pathological lipid expression in the App$^{NL\text{-}G\text{-}F}$ and h-Aβ mouse models. We employed unbiased network analysis to identify specific lipid co-expression modules (PEMs) co-localized with amyloid plaques in the App$^{NL\text{-}G\text{-}F}$ model. These mouse PEMs comprised lysophospholipids (LPCs, LPAs, LPGs, and LPIs), BMPs, and polyunsaturated PGs. Their focal accumulation was age-dependent and associated with markers of microglial inflammatory activation (CD68+) or phagocytosis (LAMP1+).

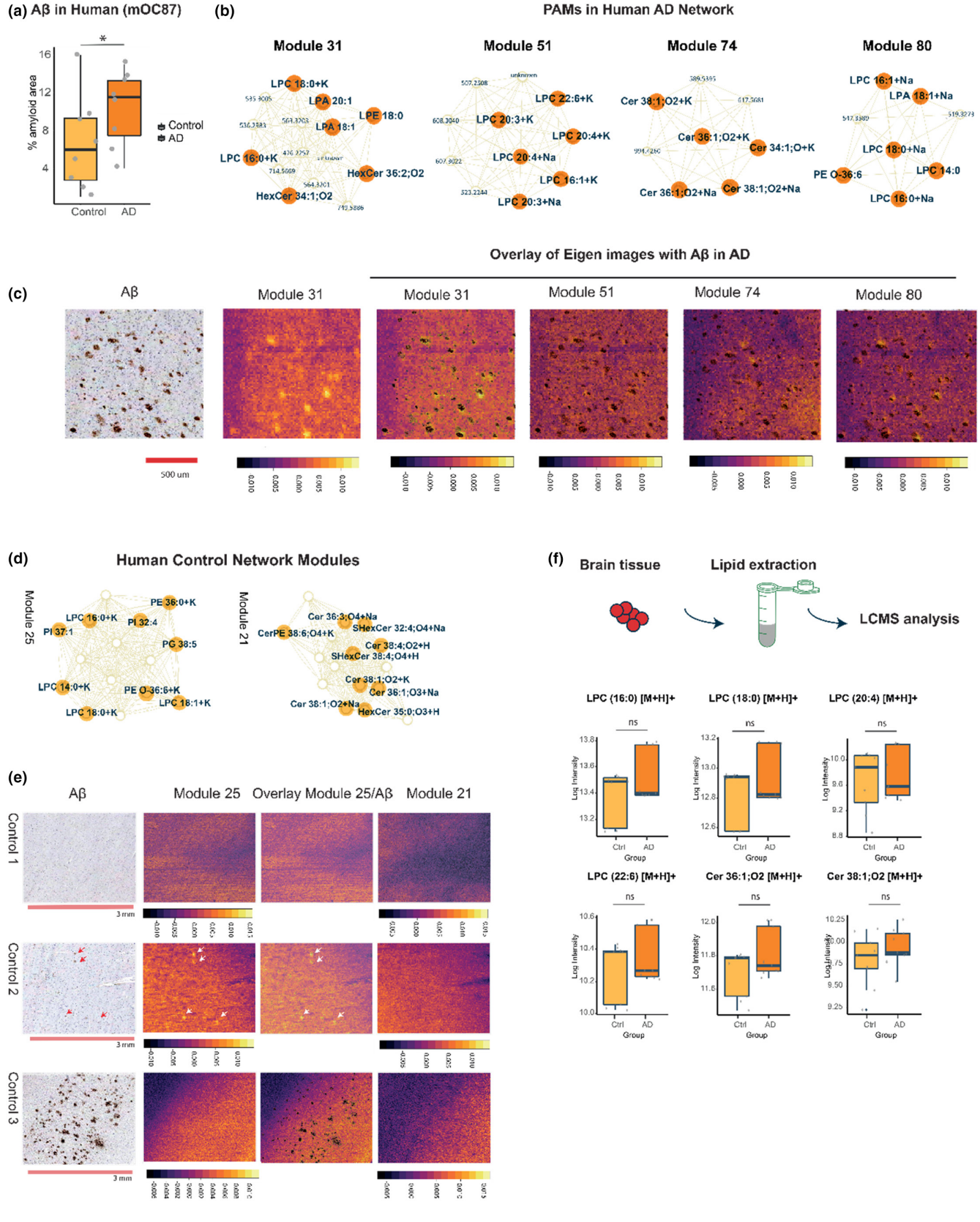

We then tested for the expression of similar plaques enriched lipids in human AD and non-diseased control cortical tissues at a spatial resolution (25 μm) sufficient to resolve mid-sized and larger human plaques. Our results showed that Aβ plaques in AD donors were also variably associated with focal accumulations of lipids, including LPCs, LPAs, Cers, and HexCers. In contrast, the diffuse Aβ plaques found in most (7/8) of the non-diseased control human brain sections were not associated with plaque-associated lipid

FIGURE 8 Lipid Expression Patterns in Human AD Brains Co-localized with β-Amyloid Plaques. (a) Assessment of total mOC87 amyloid burden in human brain samples from non-diseased controls ($n=8$) and AD cases ($n=7$). Quantification was performed using nine sections from each subject, with individual data points representing measurements from each subject. (b) Identification of four distinct modules associated with plaques in the AD lipidomic SNN network. (c) Visualization of eigen-images corresponding to four plaque-enriched modules (PEMs) lipids identified in AD, superimposed on amyloid staining. (d) Distribution of LPC (18:0), LPC (16:0), and Cer (38:1) in module 25 and module 21 of the control SNN lipidomic network. (e) Overlay of eigen images from modules 21 and 25 with amyloid staining in three selected control cases. Case 1 is amyloid-free, case 2 displays few small plaques, and control 3 exhibits the highest amyloid load. Case 2 demonstrated limited lipid puncta in module 25 that can be co-localized with amyloid plaques. (f) Quantitative analysis of module-specific lipid content relevant to plaque formation was conducted through extraction-based LCMS analysis ($n=3$). No statistically significant differences were observed, potentially attributed to the limited sample size.

co-expression. These results emphasize that the lipidomic changes related to the progression of Aβ pathology in both mouse models and human AD are spatially heterogeneous and, in human tissue, appear specific to AD. In conjunction with the mouse model data, they provide evidence that plaque-associated disruption of lipid homeostasis evolves dynamically with the local glial inflammatory response.

Previous lipidomic studies using bulk tissue extraction-based MS methods have shown lipid profile differences in mouse models (Palavicini et al., 2017; Xia et al., 2022), human AD (Chan et al., 2012; Lefterov et al., 2019), and in the context of aging (Svennerholm et al., 1994). MALDI MSI studies in aged tgArcSwe and 5xFAD mice demonstrated the spatial co-localization of lysophospholipids and other lipid species with Aβ (Ge et al., 2023; Kaya et al., 2018b, 2020; Michno et al., 2018, 2019). In tgAPPSwe and tgAPPArcSwe mice, lipid species such as gangliosides, phosphoinositols, conjugated ceramides, and lysophospholipids, including the LPCs, LPAs, and LPIs, were associated with different stages of plaque evolution (Ge, Koutarapu, et al., 2023). Cers were suggested to play a role in initial plaque seeding or amyloid maturation based on these mouse model data (Ge, Koutarapu, et al., 2023). Our findings in AD highlight a specific relationship between Cers and amyloid plaques at higher Braak stages, while lysophospholipids such as LPCs may be associated with plaques at both early and late Braak stages.

Lysophospholipid accumulation provides a metabolic marker for activating PLA2, which generates LPLs and inflammatory mediators (e.g., arachidonic acid, DHA) from membrane phospholipids and sphingolipids (Sato et al., 2016). Lysophospholipids are biologically active and modulate membrane-associated enzymes and growth factors (Sun et al., 2021). We believe that the high abundance of LPCs in the ventricle wall may be a consequence of the high expression of major facilitator superfamily domain-containing protein 2a (MFSD2A), a lysolipid transporter of docosahexaenoic acid (DHA) and other polyunsaturated fatty acids (PUFAs) at the CSF–brain barrier (Nguyen et al., 2014; Wong et al., 2016). Perturbation of lipidomic homeostasis, resulting in the accumulation of excessive LPLs, was reported previously with APP over-expression in Aβ transgenic mice (Palavicini et al., 2017). Our observations in the $App^{NL\text{-}G\text{-}F}$ mice, where human mutated APP is expressed under the control of the endogenous promoter, confirm that these lipidomic changes are not an artifact of over-expression but reflect the consequences of Aβ aggregates' deposition.

Immunohistology of sections after DESI MSI revealed the co-localization of BMPs and polyunsaturated PGs with Aβ plaques, consistent with their association with endolysosomes (Showalter et al., 2020), as PG is regarded the endogenous precursor for de novo BMP biosynthesis (Gallala & Sandhoff, 2011; Showalter et al., 2020). PGs also can be precursors to cardiolipin for synthesis in the mitochondria (Ellis et al., 2005; Nguyen et al., 2016). PAs can be used to generate PG and increases of PAs in plaques have been reported previously (Tian et al., 2019). We also showed that increased expression of these and other PEM lipids is not unique to the brains of the $App^{NL\text{-}G\text{-}F}$ mice, although their co-localization as a discrete spatial co-expression module is. They were found with other lipids distributed across two different and spatially more diffusely distributed modules in the WT and h-Aβ mice. The spatial lipidome networks in h-Aβ and WT mice described regionally distinct co-expression patterns for BMPs and LPIs. Bulk lipidomic analyses confirmed a global up-regulation of LPLs and BMP (44:12) in the h-Aβ mice compared to the WT mice, similar to that found in the $App^{NL\text{-}G\text{-}F}$ mice. The spatial and bulk information together established that these biochemical changes are expressed with early Aβ pathology in the mice. We also showed that BMP levels in the gray matter of human cortical sections at the early Braak stage (0-II) were higher than that of the gray matter at the late stages (Braak V-VI).

The age-related changes in the $App^{NL\text{-}G\text{-}F}$ mouse model and evidence for differences in lipid module co-expression with Aβ plaques at early and late Braak stages. For example, although we did not find focal pro-inflammatory lipid accumulation or increased $CD68^{+}$ microglia expression associated with plaques at 2.5 months in the $App^{NL\text{-}G\text{-}F}$ mice, these were commonly related to plaques at 7 and 12 months. This is consistent with previous studies showing that the age-dependent evolution of plaques is associated with increased CD68+ and microglial amyloid phagocytosis (Benitez et al., 2021; Michno et al., 2021). Evidence consistent with a similar evolution also was seen in the human sections, as double labeling demonstrated that the fractions of diffuse (which did not show enrichment in PEM lipids or BMPs), fibrillar, and dense-cored plaques (which showed this enrichment) increased several-fold in comparisons between early and late-stage AD (Dickson & Vickers, 2001). These observations suggest that patterns of lipid co-expression could provide an index to the stage of evolution of plaques.

Spatial lipidomic observations will contribute to more specific interpretations of lipid measures in tissue and blood. The increase of HexCers in AD blood has been reported widely and suggested as

a possible biomarker (Huynh et al., 2020). Here, we highlight a relative depletion of several HexCers in mouse plaques, consistent with previous MSI-based observations made in familial AD mice (Kaya et al., 2020). However, we also found that they were increased in deep cortical layers with AD, which could explain their global upregulation in bulk lipidomic analyses (Dehghan et al., 2022). The increase thus reflects lipid changes in a specific tissue compartment, mechanisms responsible for which will need further study.

A prognostic potential of lipid biomarkers for AD has been suggested. For example, concentrations of LPC (18:2) in peripheral blood allow the prediction of conversion to AD within 2–3 years (Mapstone et al., 2014). CSF C18 ceramide concentrations distinguish AD and non-diseased control tissues, and another untargeted study has shown that concentrations of a set of lipids, including PCs, PEs, and cholesterols in the CSF also can distinguish between people with AD and controls (Byeon et al., 2021a). Differential association of BMP, ceramides, and other PEM lipids with stages of evolution of Aβ plaques may help to explain this (Liu et al., 2021). Based on our work here, we hypothesize that soluble lipids could provide an index of the evolution of Aβ pathology sensitive to the transition from the forms of "benign" plaques found in non-diseased controls and early AD.

Nonetheless, we are mindful of the limitations of our study. The absence of an internal standard across all DESI experiments in this initial exploratory study prevented us from assessing the absolute intensity levels of ions. It limited the normalization of observations across samples. The generalizability of our findings to independent samples will require further validation with larger sample sizes of pre-clinical models at different ages and human tissues with various stages of pathology, including observations across different regions of the same brains. The unexpected differences in lipid composition between h-Aβ and WT mouse brains may be influenced by factors such as diet or environment, warranting additional studies using animals raised together to confirm the observed differences. Finally, we used were from snap frozen tissues as described in several previous studies (Kaya et al., 2017, 2018a; Michno et al., 2018, 2022), although some reports have emphasized the need for more rapid fixation using high-energy microwave-based fixation in situ to arrest metabolism more rapidly (Juras et al., 2023; Murphy, 2010). Instead, we worked to mitigate any effects of residual enzymatic activity for the conclusions here by careful standardization of the protocol across all groups being prepared, rapid vacuum desiccation after sample freezing, and using methanol as a solvent for the DESI MSI, so we believe that relative differences are meaningful.

Our study utilized spatial lipidome profiling with DESI-MSI to characterize age-dependent biochemical alterations in the amyloid plaque microenvironment. We provided evidence for the generation of lipid species with the potential to modulate glial inflammatory activation associated with amyloid plaques in AD. The differential associations of specific brain lipid species with Aβ pathology and stages and their correlations with biomarkers in CSF also offer a framework for interpreting lipid biomarkers in AD regarding the evolution of Aβ plaque pathology.

AUTHOR CONTRIBUTIONS

Helen Xuexia Huang: Investigation; methodology; validation; visualization; writing – original draft. **Paolo Inglese:** Data curation; formal analysis; software; validation; visualization; writing – review and editing. **Jiabin Tang:** Investigation; methodology. **Gonçalo Correia:** Data curation; formal analysis. **Riad Yagoubi:** Investigation; methodology. **Stephane Camuzeaux:** Investigation; methodology; writing – review and editing. **Verena M. Horneffer-van der Sluis:** Methodology. **Vincen Wu:** Methodology. **Maksym Kopanitsa:** Project administration; resources; writing – review and editing. **Nanet Willumsen:** Resources. **Johanna Jackson:** Resources. **Anna M Barron:** Resources. **Takaomi C. Saido:** Resources. **Takashi Saito:** Resources. **Steve Gentleman:** Resources; supervision. **Zoltan Takats:** Conceptualization; funding acquisition; project administration; supervision; writing – review and editing. **Paul Matthews:** Conceptualization; funding acquisition; project administration; resources; supervision; writing – review and editing.

ACKNOWLEDGMENTS

We thank the donors and their families for the use of human brain tissue in this study and the UK brain bank staff for making it available. Tissue for this study was provided by the Newcastle Brain Tissue Resource which is founded in party by a grant from the UK Medical Research Council (G0400074), by NIHR Newcastle Biomedical Research Centre and Unit awarded to the Newcastle upon Tyne NHS Foundation Trust and Newcastle University, and as part of the Brains for Dementia Research Programme jointly funded by Alzheimer's Research UK and Alzheimer's Society. We thank Dr. Lutgarde Serneels from Prof Bart De Strooper's group for providing us with h- Aβ mice samples and Prof. Anna Barron's lab for providing the App^{NL-G-F} mice, originally from Drs. Takaomi Saido (RIKEN Center for Brain Science) and Takashi Saito (Nagoya City University Graduate School of Medical Sciences). This research was supported by the Newcastle tissue bank, from which we obtained fresh frozen human tissues. The LCMS experiments were carried out using facilities at the National Phenome Centre within the Division of Systems Medicine in the Department of Metabolism, Digestion and Reproduction at Imperial College London, which is supported by the National Institute for Health Research (NIHR) Imperial Biomedical Research Centre (BRC). PMM acknowledges additional support from the Edmond J. Safra Foundation and Lily Safra, an NIHR Senior Investigator Award, and the Imperial College Healthcare Trust (ICHT) NIHR Biomedical Research Centre.

FUNDING INFORMATION

This work is funded by the UK Dementia Research Institute (to PMM), which receives funding from UK DRI Ltd, funded by the UK Medical Research Council, Alzheimer's Society, and Alzheimer's Research UK.

CONFLICT OF INTEREST STATEMENT

PMM has received consultancy fees from Novartis, Nodthera, and Biogen. He has received honoraria or speakers' fees from Novartis,

Astex, and Biogen and research or educational funds from Biogen, Novartis, Merck, and Bristol Myers Squibb.

PEER REVIEW

The peer review history for this article is available at https://www.webofscience.com/api/gateway/wos/peer-review/10.1111/jnc.16042.

DATA AVAILABILITY STATEMENT

All raw LC–MS data are publicly available on the Metabolights repository (https://www.ebi.ac.uk/metabolights/MTBLS551/). All DESI MSI raw data are available on the METASPACE (https://metaspace2020.eu/). This paper does not report the original code.

ORCID

Helen Xuexia Huang https://orcid.org/0000-0002-4109-4512
Anna M. Barron https://orcid.org/0000-0002-4715-9364
Paul M. Matthews https://orcid.org/0000-0002-1619-8328

REFERENCES

Aichler, M., & Walch, A. (2015). MALDI imaging mass spectrometry: Current frontiers and perspectives in pathology research and practice. *Laboratory Investigation*, *95*(4), 422–431.

Akyol, S., Ugur, Z., Yilmaz, A., Ustun, I., Gorti, S. K. K., Oh, K., McGuinness, B., Passmore, P., Kehoe, P. G., Maddens, M. E., Green, B. D., & Graham, S. F. (2021). Lipid profiling of Alzheimer's disease brain highlights enrichment in glycerol(phospho)lipid, and sphingolipid metabolism. *Cell*, *10*(10), 2591.

Ambrose, S., Housden, N. G., Gupta, K., Fan, J., White, P., Yen, H. Y., Marcoux, J., Kleanthous, C., Hopper, J. T. S., & Robinson, C. V. (2017). Native desorption electrospray ionization liberates soluble and membrane protein complexes from surfaces. *Angewandte Chemie (International Ed. in English)*, *56*(46), 14463–14468.

Anderson, D. M. G., Ablonczy, Z., Koutalos, Y., Hanneken, A. M., Spraggins, J. M., Calcutt, M. W., Crouch, R. K., Caprioli, R. M., & Schey, K. L. (2017). Bis(monoacylglycero)phosphate lipids in the retinal pigment epithelium implicate lysosomal/endosomal dysfunction in a model of Stargardt disease and human retinas. *Scientific Reports*, *7*(1), 17352.

Baglietto-Vargas, D., Forner, S., Cai, L., Martini, A. C., Trujillo-Estrada, L., Swarup, V., Nguyen, M. M. T., do Huynh, K., Javonillo, D. I., Tran, K. M., Phan, J., Jiang, S., Kramár, E. A., Nuñez-Diaz, C., Balderrama-Gutierrez, G., Garcia, F., Childs, J., Rodriguez-Ortiz, C. J., Garcia-Leon, J. A., … LaFerla, F. M. (2021). Generation of a humanized Abeta expressing mouse demonstrating aspects of Alzheimer's disease-like pathology. *Nature Communications*, *12*(1), 2421.

Barupal, D. K., Baillie, R., Fan, S., Saykin, A. J., Meikle, P. J., Arnold, M., Nho, K., Fiehn, O., Kaddurah-Daouk, R., Alzheimer's Disease Neuroimaging Initiative, & Alzheimer Disease Metabolomics Consortium. (2019). Sets of coregulated serum lipids are associated with Alzheimer's disease pathophysiology. *Alzheimers Dement (Amst)*, *11*, 619–627.

Bates, D. (2010). *lme4: Linear mixed-effects models using S4 classes*. http://CRAN.R-project.org/package=lme4

Benitez, D. P., Jiang, S., Wood, J., Wang, R., Hall, C. M., Peerboom, C., Wong, N., Stringer, K. M., Vitanova, K. S., Smith, V. C., Joshi, D., Saito, T., Saido, T. C., Hardy, J., Hanrieder, J., de Strooper, B., Salih, D. A., Tripathi, T., Edwards, F. A., & Cummings, D. M. (2021). Knock-in models related to Alzheimer's disease: Synaptic transmission, plaques and the role of microglia. *Molecular Neurodegeneration*, *16*(1), 47.

Berman, D. E., Dall'Armi, C., Voronov, S. V., McIntire, L. B. J., Zhang, H., Moore, A. Z., Staniszewski, A., Arancio, O., Kim, T. W., & di Paolo, G. (2008). Oligomeric amyloid-beta peptide disrupts phosphatidylinositol-4,5-bisphosphate metabolism. *Nature Neuroscience*, *11*(5), 547–554.

Bertrand, P., Poirier, J., Oda, T., Finch, C. E., & Pasinetti, G. M. (1995). Association of apolipoprotein E genotype with brain levels of apolipoprotein E and apolipoprotein J (clusterin) in Alzheimer disease. *Brain Research. Molecular Brain Research*, *33*(1), 174–178.

Bolte, S., & Cordelieres, F. P. (2006). A guided tour into subcellular colocalization analysis in light microscopy. *Journal of Microscopy*, *224*, 213–232.

Byeon, S. K., Madugundu, A. K., Jain, A. P., Bhat, F. A., Jung, J. H., Renuse, S., Darrow, J., Bakker, A., Albert, M., Moghekar, A., & Pandey, A. (2021a). Cerebrospinal fluid lipidomics for biomarkers of Alzheimer's disease. *Molecular Omics*, *17*(3), 454–463.

Chambers, M. C., Maclean, B., Burke, R., Amodei, D., Ruderman, D. L., Neumann, S., Gatto, L., Fischer, B., Pratt, B., Egertson, J., Hoff, K., Kessner, D., Tasman, N., Shulman, N., Frewen, B., Baker, T. A., Brusniak, M. Y., Paulse, C., Creasy, D., … Mallick, P. (2012). A cross-platform toolkit for mass spectrometry and proteomics. *Nature Biotechnology*, *30*(10), 918–920.

Chan, R. B., Oliveira, T. G., Cortes, E. P., Honig, L. S., Duff, K. E., Small, S. A., Wenk, M. R., Shui, G., & di Paolo, G. (2012). Comparative lipidomic analysis of mouse and human brain with Alzheimer disease. *The Journal of Biological Chemistry*, *287*(4), 2678–2688.

Cleveland, W. S., & Devlin, S. J. (1988). Locally weighted regression: An approach to regression analysis by local fitting. *Journal of the American Statistical Association*, *83*(403), 596–610.

Dahlgren, K. N., Manelli, A. M., Stine, W. B., Jr., Baker, L. K., Krafft, G. A., & LaDu, M. J. (2002). Oligomeric and fibrillar species of amyloid-beta peptides differentially affect neuronal viability. *The Journal of Biological Chemistry*, *277*(35), 32046–32053.

Dannhorn, A., Kazanc, E., Ling, S., Nikula, C., Karali, E., Serra, M. P., Vorng, J. L., Inglese, P., Maglennon, G., Hamm, G., Swales, J., Strittmatter, N., Barry, S. T., Sansom, O. J., Poulogiannis, G., Bunch, J., Goodwin, R. J. A., & Takats, Z. (2020). Universal sample preparation unlocking multimodal molecular tissue imaging. *Analytical Chemistry*, *92*(16), 11080–11088.

Dehghan, A., Pinto, R. C., Karaman, I., Huang, J., Durainayagam, B. R., Ghanbari, M., Nazeer, A., Zhong, Q., Liggi, S., Whiley, L., Mustafa, R., Kivipelto, M., Solomon, A., Ngandu, T., Kanekiyo, T., Aikawa, T., Radulescu, C. I., Barnes, S. J., Graça, G., … Elliott, P. (2022). Metabolome-wide association study on ABCA7 indicates a role of ceramide metabolism in Alzheimer's disease. *Proceedings of the National Academy of Sciences of the United States of America*, *119*(43), e2206083119.

Depp, C., Sun, T., Sasmita, A. O., Spieth, L., Berghoff, S. A., Nazarenko, T., Overhoff, K., Steixner-Kumar, A. A., Subramanian, S., Arinrad, S., Ruhwedel, T., Möbius, W., Göbbels, S., Saher, G., Werner, H. B., Damkou, A., Zampar, S., Wirths, O., Thalmann, M., … Nave, K. A. (2023). Myelin dysfunction drives amyloid-beta deposition in models of Alzheimer's disease. *Nature*, *618*(7964), 349–357.

Deutsch, E. W. (2010). Mass spectrometer output file format mzML. *Methods in Molecular Biology*, *604*, 319–331.

Dickson, T. C., & Vickers, J. C. (2001). The morphological phenotype of beta-amyloid plaques and associated neuritic changes in Alzheimer's disease. *Neuroscience*, *105*(1), 99–107.

Dieterle, F., Ross, A., Schlotterbeck, G., & Senn, H. (2006). Probabilistic quotient normalization as robust method to account for dilution of complex biological mixtures. Application in 1H NMR metabonomics. *Analytical Chemistry*, *78*(13), 4281–4290.

Domingues, P., Domingues, M. R. M., Amado, F. M. L., & Ferrer-Correia, A. J. (2001). Characterization of sodiated glycerol phosphatidylcholine

phospholipids by mass spectrometry. *Rapid Communications in Mass Spectrometry*, *15*(10), 799–804.

Dutta, A., & Zisserman, A. (2019). The VIA annotation software for images, audio and video. In *Proceedings of the 27th ACM international conference on multimedia* (pp. 2276–2279). Association for Computing Machinery.

Ellis, C. E., Murphy, E. J., Mitchell, D. C., Golovko, M. Y., Scaglia, F., Barceló-Coblijn, G. C., & Nussbaum, R. L. (2005). Mitochondrial lipid abnormality and electron transport chain impairment in mice lacking alpha-synuclein. *Molecular and Cellular Biology*, *25*(22), 10190–10201.

Fitzner, D., Bader, J. M., Penkert, H., Bergner, C. G., Su, M., Weil, M. T., Surma, M. A., Mann, M., Klose, C., & Simons, M. (2020). Cell-type- and brain-region-resolved mouse brain lipidome. *Cell Reports*, *32*(11), 108132.

Folch, J., Lees, M., & Stanley, G. S. (1957). A simple method for the isolation and purification of total lipides from animal tissues. *Journal of Biological Chemistry*, *226*(1), 497–509.

Fonteh, A. N., Chiang, A. J., Arakaki, X., Edminster, S. P., & Harrington, M. G. (2020). Accumulation of cerebrospinal fluid Glycerophospholipids and sphingolipids in cognitively healthy participants with Alzheimer's biomarkers precedes lipolysis in the dementia stage. *Frontiers in Neuroscience*,*14: 611393*.

Gallala, H. D., & Sandhoff, K. (2011). Biological function of the cellular lipid BMP-BMP as a key activator for cholesterol sorting and membrane digestion. *Neurochemical Research*, *36*(9), 1594–1600.

Gao, Y., Layritz, C., Legutko, B., Eichmann, T. O., Laperrousaz, E., Moullé, V. S., Cruciani-Guglielmacci, C., Magnan, C., Luquet, S., Woods, S. C., Eckel, R. H., Yi, C. X., Garcia-Caceres, C., & Tschöp, M. H. (2017). Disruption of lipid uptake in Astroglia exacerbates diet-induced obesity. *Diabetes*, *66*(10), 2555–2563.

Gazos-Lopes, F., Oliveira, M. M., Hoelz, L. V. B., Vieira, D. P., Marques, A. F., Nakayasu, E. S., Gomes, M. T., Salloum, N. G., Pascutti, P. G., Souto-Padrón, T., Monteiro, R. Q., Lopes, A. H., & Almeida, I. C. (2014). Structural and functional analysis of a platelet-activating lysophosphatidylcholine of Trypanosoma cruzi. *PLoS Neglected Tropical Diseases*, *8*(8), e3077.

Ge, J., Koutarapu, S., Jha, D., Dulewicz, M., Zetterberg, H., Blennow, K., & Hanrieder, J. (2023). Tetramodal chemical imaging delineates the lipid-amyloid peptide interplay at single plaques in transgenic Alzheimer's disease models. *Analytical Chemistry*, *95*(10), 4692–4702.

Gibb, S., & Strimmer, K. (2012). MALDIquant: A versatile R package for the analysis of mass spectrometry data. *Bioinformatics*, *28*(17), 2270–2271.

Guo, N., van Unen, V., Ijsselsteijn, M. E., Ouboter, L. F., van der Meulen, A. E., Chuva de Sousa Lopes, S. M., de Miranda, N. F. C. C., Koning, F., & Li, N. (2020). A 34-marker panel for imaging mass cytometric analysis of human snap-frozen tissue. *Frontiers in Immunology*, *11*(1466), 548984.

Hatami, A., Albay, R., III, Monjazeb, S., Milton, S., & Glabe, C. (2014). Monoclonal antibodies against Abeta42 fibrils distinguish multiple aggregation state polymorphisms in vitro and in Alzheimer disease brain. *The Journal of Biological Chemistry*, *289*(46), 32131–32143.

Huynh, K., Lim, W. L. F., Giles, C., Jayawardana, K. S., Salim, A., Mellett, N. A., Smith, A. A. T., Olshansky, G., Drew, B. G., Chatterjee, P., Martins, I., Laws, S. M., Bush, A. I., Rowe, C. C., Villemagne, V. L., Ames, D., Masters, C. L., Arnold, M., Nho, K., … Meikle, P. J. (2020). Concordant peripheral lipidome signatures in two large clinical studies of Alzheimer's disease. *Nature Communications*, *11*(1), 5698.

Inglese, P., Correia, G., Takats, Z., Nicholson, J. K., & Glen, R. C. (2019). SPUTNIK: An R package for filtering of spatially related peaks in mass spectrometry imaging data. *Bioinformatics*, *35*(1), 178–180.

Inglese, P., et al. (2018). *Network analysis of mass spectrometry imaging data from colorectal cancer identifies key metabolites common to metastatic development*. *bioRxiv* 230052.

Inglese, P., et al. (2021). Mass recalibration for desorption electrospray ionization mass spectrometry imaging using endogenous reference ions. *bioRxiv*.

Iwamoto, N., Nishiyama, E., Ohwada, J., & Arai, H. (1997). Distribution of amyloid deposits in the cerebral white matter of the Alzheimer's disease brain: Relationship to blood vessels. *Acta Neuropathologica*, *93*(4), 334–340.

Izzi-Engbeaya, C., Comninos, A. N., Clarke, S. A., Jomard, A., Yang, L., Jones, S., Abbara, A., Narayanaswamy, S., Eng, P. C., Papadopoulou, D., Prague, J. K., Bech, P., Godsland, I. F., Bassett, P., Sands, C., Camuzeaux, S., Gomez-Romero, M., Pearce, J. T. M., Lewis, M. R., … Dhillo, W. S. (2018). The effects of kisspeptin on beta-cell function, serum metabolites and appetite in humans. *Diabetes, Obesity & Metabolism*, *20*(12), 2800–2810.

Jansen, I. E., Savage, J. E., Watanabe, K., Bryois, J., Williams, D. M., Steinberg, S., Sealock, J., Karlsson, I. K., Hägg, S., Athanasiu, L., Voyle, N., Proitsi, P., Witoelar, A., Stringer, S., Aarsland, D., Almdahl, I. S., Andersen, F., Bergh, S., Bettella, F., … Posthuma, D. (2019). Genome-wide meta-analysis identifies new loci and functional pathways influencing Alzheimer's disease risk. *Nature Genetics*, *51*(3), 404–413.

Juras, J. A., Webb, M. B., Young, L. E. A., Markussen, K. H., Hawkinson, T. R., Buoncristiani, M. D., Bolton, K. E., Coburn, P. T., Williams, M. I., Sun, L. P. Y., Sanders, W. C., Bruntz, R. C., Conroy, L. R., Wang, C., Gentry, M. S., Smith, B. N., & Sun, R. C. (2023). In situ microwave fixation provides an instantaneous snapshot of the brain metabolome. *Cell Reports Methods*, *3*(4), 100455.

Kaya, I., Brinet, D., Michno, W., Başkurt, M., Zetterberg, H., Blenow, K., & Hanrieder, J. (2017). Novel trimodal MALDI imaging mass spectrometry (IMS3) at 10 mum reveals spatial lipid and peptide correlates implicated in Abeta plaque pathology in Alzheimer's disease. *ACS Chemical Neuroscience*, *8*(12), 2778–2790.

Kaya, I., Jennische, E., Lange, S., Tarik Baykal, A., Malmberg, P., & Fletcher, J. S. (2020). Brain region-specific amyloid plaque-associated myelin lipid loss, APOE deposition and disruption of the myelin sheath in familial Alzheimer's disease mice. *Journal of Neurochemistry*, *154*(1), 84–98.

Kaya, I., Nilsson, A., Luptáková, D., He, Y., Vallianatou, T., Bjärterot, P., Svenningsson, P., Bezard, E., & Andrén, P. E. (2023). Spatial lipidomics reveals brain region-specific changes of sulfatides in an experimental MPTP Parkinson's disease primate model. *NPJ Parkinsons Disease*, *9*(1), 118.

Kaya, I., Zetterberg, H., Blennow, K., & Hanrieder, J. (2018a). Shedding light on the molecular pathology of amyloid plaques in transgenic Alzheimer's disease mice using multimodal MALDI imaging mass spectrometry. *ACS Chemical Neuroscience*, *9*(7), 1802–1817.

Kirilina, E., Helbling, S., Morawski, M., Pine, K., Reimann, K., Jankuhn, S., Dinse, J., Deistung, A., Reichenbach, J. R., Trampel, R., Geyer, S., Müller, L., Jakubowski, N., Arendt, T., Bazin, P. L., & Weiskopf, N. (2020). Superficial white matter imaging: Contrast mechanisms and whole-brain in vivo mapping. *Science Advances*, *6*(41), aaz9281.

Langfelder, P., & Horvath, S. (2007). Eigengene networks for studying the relationships between co-expression modules. *BMC Systems Biology*, *1*(1), 54.

Langfelder, P., Zhang, B., & Horvath, S. (2008). Defining clusters from a hierarchical cluster tree: The dynamic tree cut package for R. *Bioinformatics*, *24*(5), 719–720.

Lefterov, I., Wolfe, C. M., Fitz, N. F., Nam, K. N., Letronne, F., Biedrzycki, R. J., Kofler, J., Han, X., Wang, J., Schug, J., & Koldamova, R. (2019). APOE2 orchestrated differences in transcriptomic and lipidomic profiles of postmortem AD brain. *Alzheimer's Research & Therapy*, *11*(1), 113.

Lenth, R., et al. (2019). *Package 'emmeans'*.

Lenth, R. V. (2021). Emmeans: Estimated marginal means, aka least-squares means. R package version 1.5.4.

Lewis, M., et al., *An open platform for large scale LC-MS-based metabolomics*. 2022, ChemRxiv.

Lichtenthaler, S. F., Wang, R., Grimm, H., Uljon, S. N., Masters, C. L., & Beyreuther, K. (1999). Mechanism of the cleavage specificity of Alzheimer's disease gamma-secretase identified by phenylalanine-scanning mutagenesis of the transmembrane domain of the amyloid precursor protein. *Proceedings of the National Academy of Sciences of the United States of America*, *96*(6), 3053–3058.

Liu, Y., Thalamuthu, A., Mather, K. A., Crawford, J., Ulanova, M., Wong, M. W. K., Pickford, R., Sachdev, P. S., & Braidy, N. (2021). Plasma lipidome is dysregulated in Alzheimer's disease and is associated with disease risk genes. *Translational Psychiatry*, *11*(1), 344.

Mace, S., et al. (2005). ABCA2 is a strong genetic risk factor for early-onset Alzheimer's disease. *Neurobiology of Disease*, *18*(1), 119–125.

Mahley, R. W., Weisgraber, K. H., & Huang, Y. (2006). Apolipoprotein E4: A causative factor and therapeutic target in neuropathology, including Alzheimer's disease. *Proceedings of the National Academy of Sciences of the United States of America*, *103*(15), 5644–5651.

Mapstone, M., Cheema, A. K., Fiandaca, M. S., Zhong, X., Mhyre, T. R., MacArthur, L. H., Hall, W. J., Fisher, S. G., Peterson, D. R., Haley, J. M., Nazar, M. D., Rich, S. A., Berlau, D. J., Peltz, C. B., Tan, M. T., Kawas, C. H., & Federoff, H. J. (2014). Plasma phospholipids identify antecedent memory impairment in older adults. *Nature Medicine*, *20*(4), 415–418.

Michno, W., Kaya, I., Nyström, S., Guerard, L., Nilsson, K. P. R., Hammarström, P., Blennow, K., Zetterberg, H., & Hanrieder, J. (2018). Multimodal chemical imaging of amyloid plaque polymorphism reveals Abeta aggregation dependent anionic lipid accumulations and metabolism. *Analytical Chemistry*, *90*(13), 8130–8138.

Michno, W., Stringer, K. M., Enzlein, T., Passarelli, M. K., Escrig, S., Vitanova, K., Wood, J., Blennow, K., Zetterberg, H., Meibom, A., Hopf, C., Edwards, F. A., & Hanrieder, J. (2021). Following spatial Abeta aggregation dynamics in evolving Alzheimer's disease pathology by imaging stable isotope labeling kinetics. *Science Advances*, *7*(25), eabg4855.

Michno, W., Wehrli, P. M., Blennow, K., Zetterberg, H., & Hanrieder, J. (2019). Molecular imaging mass spectrometry for probing protein dynamics in neurodegenerative disease pathology. *Journal of Neurochemistry*, *151*(4), 488–506.

Michno, W., Wehrli, P. M., Koutarapu, S., Marsching, C., Minta, K., Ge, J., Meyer, S. W., Zetterberg, H., Blennow, K., Henkel, C., Oetjen, J., Hopf, C., & Hanrieder, J. (2022). Structural amyloid plaque polymorphism is associated with distinct lipid accumulations revealed by trapped ion mobility mass spectrometry imaging. *Journal of Neurochemistry*, *160*(4), 482–498.

Miller, Y. I., Navia-Pelaez, J. M., Corr, M., & Yaksh, T. L. (2020). Lipid rafts in glial cells: Role in neuroinflammation and pain processing. *Journal of Lipid Research*, *61*(5), 655–666.

Murphy, E. J. (2010). Brain fixation for analysis of brain lipid-mediators of signal transduction and brain eicosanoids requires head-focused microwave irradiation: An historical perspective. *Prostaglandins & Other Lipid Mediators*, *91*(3–4), 63–67.

Nguyen, H. M., Mejia, E. M., Chang, W., Wang, Y., Watson, E., On, N., Miller, D. W., & Hatch, G. M. (2016). Reduction in cardiolipin decreases mitochondrial spare respiratory capacity and increases glucose transport into and across human brain cerebral microvascular endothelial cells. *Journal of Neurochemistry*, *139*(1), 68–80.

Nguyen, L. N., Ma, D., Shui, G., Wong, P., Cazenave-Gassiot, A., Zhang, X., Wenk, M. R., Goh, E. L. K., & Silver, D. L. (2014). Mfsd2a is a transporter for the essential omega-3 fatty acid docosahexaenoic acid. *Nature*, *509*(7501), 503.

Nielsen, M. M., et al. (2016). Mass spectrometry imaging of biomarker lipids for phagocytosis and signalling during focal cerebral ischaemia. *Scientific Reports*, *6*, 39571.

Nilsberth, C., Westlind-Danielsson, A., Eckman, C. B., Condron, M. M., Axelman, K., Forsell, C., Stenh, C., Luthman, J., Teplow, D. B., Younkin, S. G., Näslund, J., & Lannfelt, L. (2001). The 'Arctic' APP mutation (E693G) causes Alzheimer's disease by enhanced Abeta protofibril formation. *Nature Neuroscience*, *4*(9), 887–893.

Oliveira, T. G., & Di Paolo, G. (2010). Phospholipase D in brain function and Alzheimer's disease. *Biochimica et Biophysica Acta*, *1801*(8), 799–805.

Palavicini, J. P., Wang, C., Chen, L., Hosang, K., Wang, J., Tomiyama, T., Mori, H., & Han, X. (2017). Oligomeric amyloid-beta induces MAPK-mediated activation of brain cytosolic and calcium-independent phospholipase a(2) in a spatial-specific manner. *Acta Neuropathologica Communications*, *5*(1), 56.

Petit-Turcotte, C., Stohl, S. M., Beffert, U., Cohn, J. S., Aumont, N., Tremblay, M., Dea, D., Yang, L., Poirier, J., & Shachter, N. S. (2001). Apolipoprotein C-I expression in the brain in Alzheimer's disease. *Neurobiology of Disease*, *8*(6), 953–963.

Picard, C., Nilsson, N., Labonté, A., Auld, D., Rosa-Neto, P., the Alzheimer's Disease Neuroimaging Initiative, Ashton, N. J., Zetterberg, H., Blennow, K., Breitner, J. C. B., Villeneuve, S., Poirier, J., & for the PREVENT-AD research group. (2021). Apolipoprotein B is a novel marker for early tau pathology in Alzheimer's disease. *Alzheimers Dement*, *18*, 875–887.

Pinheiro, J., et al. (2017). Package 'Nlme'. linear and nonlinear mixed effects models, version. 3(1).

Proitsi, P., Kim, M., Whiley, L., Simmons, A., Sattlecker, M., Velayudhan, L., Lupton, M. K., Soininen, H., Kloszewska, I., Mecocci, P., Tsolaki, M., Vellas, B., Lovestone, S., Powell, J. F., Dobson, R. J. B., & Legido-Quigley, C. (2017). Association of blood lipids with Alzheimer's disease: A comprehensive lipidomics analysis. *Alzheimers Dement*, *13*(2), 140–151.

Ramesh, S., Govindarajulu, M., Suppiramaniam, V., Moore, T., & Dhanasekaran, M. (2018). Autotaxin(−)lysophosphatidic acid signaling in Alzheimer's disease. *International Journal of Molecular Sciences*, *19*(7), 1827.

Roussarie, J. P., Yao, V., Rodriguez-Rodriguez, P., Oughtred, R., Rust, J., Plautz, Z., Kasturia, S., Albornoz, C., Wang, W., Schmidt, E. F., Dannenfelser, R., Tadych, A., Brichta, L., Barnea-Cramer, A., Heintz, N., Hof, P. R., Heiman, M., Dolinski, K., Flajolet, M., … Greengard, P. (2020). Selective neuronal vulnerability in Alzheimer's disease: A network-based analysis. *Neuron*, *107*(5), 821, e12–835.

Saito, T., Matsuba, Y., Mihira, N., Takano, J., Nilsson, P., Itohara, S., Iwata, N., & Saido, T. C. (2014). Single app knock-in mouse models of Alzheimer's disease. *Nature Neuroscience*, *17*(5), 661–663.

Sands, C. J., Wolfer, A. M., Correia, G. D. S., Sadawi, N., Ahmed, A., Jiménez, B., Lewis, M. R., Glen, R. C., Nicholson, J. K., & Pearce, J. T. M. (2019). The nPYc-toolbox, a python module for the pre-processing, quality-control and analysis of metabolic profiling datasets. *Bioinformatics*, *35*(24), 5359–5360.

Sano, O., Tsujita, M., Shimizu, Y., Kato, R., Kobayashi, A., Kioka, N., Remaley, A. T., Michikawa, M., Ueda, K., & Matsuo, M. (2016). ABCG1 and ABCG4 suppress gamma-secretase activity and amyloid beta production. *PLoS One*, *11*(5), e0155400.

Sasaguri, H., Nilsson, P., Hashimoto, S., Nagata, K., Saito, T., de Strooper, B., Hardy, J., Vassar, R., Winblad, B., & Saido, T. C. (2017). APP mouse models for Alzheimer's disease preclinical studies. *The EMBO Journal*, *36*(17), 2473–2487.

Satija, R., Farrell, J. A., Gennert, D., Schier, A. F., & Regev, A. (2015). Spatial reconstruction of single-cell gene expression data. *Nature Biotechnology*, *33*(5), 495–502.

Sato, H., Taketomi, Y., & Murakami, M. (2016). Metabolic regulation by secreted phospholipase a(2). *Inflammation and Regeneration*, *36*, 7.

Satopaa, V., et al. (2011). *Finding a "Kneedle" in a Haystack: Detecting Knee Points in System Behavior. in 2011 31st International Conference on Distributed Computing Systems Workshops*.

Serneels, L., T'Syen, D., Perez-Benito, L., Theys, T., Holt, M. G., & de Strooper, B. (2020). Modeling the beta-secretase cleavage site and humanizing amyloid-beta precursor protein in rat and mouse to study Alzheimer's disease. *Molecular Neurodegeneration*, *15*(1), 60.

Shih, Y. H., Tsai, K. J., Lee, C. W., Shiesh, S. C., Chen, W. T., Pai, M. C., & Kuo, Y. M. (2014). Apolipoprotein C-III is an amyloid-beta-binding protein and an early marker for Alzheimer's disease. *Journal of Alzheimer's Disease*, *41*(3), 855–865.

Showalter, M. R., Berg, A. L., Nagourney, A., Heil, H., Carraway, K. L., III, & Fiehn, O. (2020). The emerging and diverse roles of Bis(monoacylglycero) phosphate lipids in cellular physiology and disease. *International Journal of Molecular Sciences*, *21*(21), 8067.

Slot, R. E., Van Hartenm A. C., Kester, M. I., Jongbloed, W., Bouwman, F. H., Teunissen, C. E., Scheltens, P., Veerhuis, R., & van der Flier, W. M. (2017). Apolipoprotein A1 in cerebrospinal fluid and plasma and progression to Alzheimer's disease in non-demented elderly. *Journal of Alzheimer's Disease*, *56*(2), 687–697.

Smith, C. A., Want, E. J., O'Maille, G., Abagyan, R., & Siuzdak, G. (2006). XCMS: Processing mass spectrometry data for metabolite profiling using nonlinear peak alignment, matching, and identification. *Analytical Chemistry*, *78*(3), 779–787.

Steinberg, S., et al. (2015). Loss-of-function variants in ABCA7 confer risk of Alzheimer's disease. *Nature Genetics*, *47*(5), 445 U24.

Storey, J., et al. (2015). *Package 'qvalue'*.

Strittmatter, N., Richards, F. M., Race, A. M., Ling, S., Sutton, D., Nilsson, A., Wallez, Y., Barnes, J., Maglennon, G., Gopinathan, A., Brais, R., Wong, E., Serra, M. P., Atkinson, J., Smith, A., Wilson, J., Hamm, G., Johnson, T. I., Dunlop, C. R., … Jodrell, D. I. (2022). Method to visualize the intratumor distribution and impact of gemcitabine in pancreatic ductal adenocarcinoma by multimodal imaging. *Analytical Chemistry*, *94*(3), 1795–1803.

Sturchler-Pierrat, C., Abramowski, D., Duke, M., Wiederhold, K. H., Mistl, C., Rothacher, S., Ledermann, B., Bürki, K., Frey, P., Paganetti, P. A., Waridel, C., Calhoun, M. E., Jucker, M., Probst, A., Staufenbiel, M., & Sommer, B. (1997). Two amyloid precursor protein transgenic mouse models with Alzheimer disease-like pathology. *Proceedings of the National Academy of Sciences of the United States of America*, *94*(24), 13287–13292.

Sun, G. Y., Geng, X., Teng, T., Yang, B., Appenteng, M. K., Greenlief, C. M., & Lee, J. C. (2021). Dynamic role of phospholipases A2 in health and diseases in the central nervous system. *Cell*, *10*(11), 2963.

Svennerholm, L., Boström, K., Jungbjer, B., & Olsson, L. (1994). Membrane lipids of adult human brain: Lipid composition of frontal and temporal lobe in subjects of age 20 to 100 years. *Journal of Neurochemistry*, *63*(5), 1802–1811.

Takats, Z., et al. (2004). Mass spectrometry sampling under ambient conditions with desorption electrospray ionization. *Science*, *306*(5695), 471–473.

Tian, X., Xie, B., Zou, Z., Jiao, Y., Lin, L. E., Chen, C. L., Hsu, C. C., Peng, J., & Yang, Z. (2019). Multimodal imaging of amyloid plaques: Fusion of the single-probe mass spectrometry image and fluorescence microscopy image. *Analytical Chemistry*, *91*(20), 12882–12889.

Wahrle, S. E., Jiang, H., Parsadanian, M., Kim, J., Li, A., Knoten, A., Jain, S., Hirsch-Reinshagen, V., Wellington, C. L., Bales, K. R., Paul, S. M., & Holtzman, D. M. (2008). Overexpression of ABCA1 reduces amyloid deposition in the PDAPP mouse model of Alzheimer disease. *The Journal of Clinical Investigation*, *118*(2), 671–682.

Wang, H. Y., et al. (2010). Direct profiling of phospholipids and lysophospholipids in rat brain sections after ischemic stroke. *Rapid Communications in Mass Spectrometry*, *24*(14), 2057–2064.

Wickham, H. (2011). ggplot2. *Wiley Interdisciplinary Reviews: Computational Statistics*, *3*(2), 180–185.

Wong, B. H., Chan, J. P., Cazenave-Gassiot, A., Poh, R. W., Foo, J. C., Galam, D. L. A., Ghosh, S., Nguyen, L. N., Barathi, V. A., Yeo, S. W., Luu, C. D., Wenk, M. R., & Silver, D. L. (2016). Mfsd2a is a transporter for the essential omega-3 fatty acid docosahexaenoic acid (DHA) in eye and is important for photoreceptor cell development. *Journal of Biological Chemistry*, *291*(20), 10501–10514.

Xia, D., Lianoglou, S., Sandmann, T., Calvert, M., Suh, J. H., Thomsen, E., Dugas, J., Pizzo, M. E., DeVos, S. L., Earr, T. K., Lin, C. C., Davis, S., Ha, C., Leung, A. W. S., Nguyen, H., Chau, R., Yulyaningsih, E., Lopez, I., Solanoy, H., … Sanchez, P. E. (2022). Novel app knock-in mouse model shows key features of amyloid pathology and reveals profound metabolic dysregulation of microglia. *Molecular Neurodegeneration*, *17*(1), 41.

Xiong, H. Q., et al. (2009). ABCG2 is upregulated in Alzheimer's brain with cerebral amyloid Angiopathy and may act as a gatekeeper at the blood-brain barrier for a beta(1-40) peptides. *Journal of Neuroscience*, *29*(17), 5463–5475.

Yamazaki, Y., Zhao, N., Caulfield, T. R., Liu, C. C., & Bu, G. (2019). Apolipoprotein E and Alzheimer disease: Pathobiology and targeting strategies. *Nature Reviews Neurology*, *15*(9), 501–518.

Zhu, X., Zhang, J., Xu, Y., Wang, J., Peng, X., & Li, H. D. (2020). Single-cell clustering based on shared nearest neighbor and graph partitioning. *Interdisciplinary Sciences*, *12*(2), 117–130.

Zhurov, K. O., Kozhinov, A. N., Fornelli, L., & Tsybin, Y. O. (2014). Distinguishing analyte from noise components in mass spectra of complex samples: where to cut the noise? *Analytical Chemistry*, *86*(7), 3308–3316.

SUPPORTING INFORMATION

Additional supporting information can be found online in the Supporting Information section at the end of this article.

How to cite this article: Huang, H. X., Inglese, P., Tang, J., Yagoubi, R., Correia, G. D. S., Horneffer-van der Sluis, V. M., Camuzeaux, S., Wu, V., Kopanitsa, M. V., Willumsen, N., Jackson, J. S., Barron, A. M., Saito, T., Saido, T. C., Gentlemen, S., Takats, Z., & Matthews, P. M. (2024). Mass spectrometry imaging highlights dynamic patterns of lipid co-expression with Aβ plaques in mouse and human brains. *Journal of Neurochemistry*, *168*, 1193–1214. https://doi.org/10.1111/jnc.16042